

SHOCKS AND CAVITIES FROM MULTIPLE OUTBURSTS IN THE GALAXY GROUP NGC 5813: A WINDOW TO AGN FEEDBACK

S. W. RANDALL¹, W. R. FORMAN¹, S. GIACINTUCCI^{1,2}, P. E. J. NULSEN¹, M. SUN³, C. JONES¹, E. CHURAZOV^{4,5}, L. P. DAVID¹, R. KRAFT¹, M. DONAHUE⁶, E. L. BLANTON⁷, A. SIMIONESCU⁸, N. WERNER⁸

ABSTRACT

We present results from new *Chandra*, *GMRT*, and *SOAR* observations of NGC 5813, the dominant central galaxy in a nearby galaxy group. The system shows three pairs of collinear cavities at 1 kpc, 8 kpc, and 20 kpc from the central source, from three distinct outbursts of the central AGN, which occurred 3×10^6 , 2×10^7 , and 9×10^7 yr ago. The H α and X-ray observations reveal filaments of cool gas that has been uplifted by the X-ray cavities. The inner two cavity pairs are filled with radio emitting plasma, and each pair is associated with an elliptical surface brightness edge, which we unambiguously identify as shocks (with measured temperature jumps) with Mach numbers of $M \approx 1.7$ and $M \approx 1.5$ for the inner and outer shocks, respectively. Such clear signatures from three distinct AGN outbursts in an otherwise dynamically relaxed system provide a unique opportunity to study AGN feedback and outburst history. The mean power of the two most recent outbursts differs by a factor of six, from $1.5\text{--}10 \times 10^{42}$ erg s^{−1}, indicating that the mean jet power changes significantly over long ($\sim 10^7$ yr) timescales. The total energy output of the most recent outburst is also more than an order of magnitude less than the total energy of the previous outburst (1.5×10^{56} erg versus 4×10^{57} erg), which may be a result of the lower mean power, or may indicate that the most recent outburst is ongoing. The outburst interval implied by both the shock and cavity ages ($\sim 10^7$ yr) indicates that, in this system, shock heating alone is sufficient to balance radiative cooling close to the central AGN, which is the relevant region for regulating feedback between the ICM and the central SMBH.

Subject headings: galaxies: active — galaxies: clusters: general — galaxies: groups: individual (NGC5813) — galaxies: individual (NGC5813) — X-rays: galaxies

1. INTRODUCTION

A major result from early *Chandra* and *XMM-Newton* observations was that the amount of gas in cool core clusters that cools to low temperatures is less than predicted by classical radiative cooling models (David et al. 2001; Peterson et al. 2001; Peterson & Fabian 2006). The implication is that the central gas must be re-heated. The source of this heating, and understanding when and how it takes place, has recently been a major topic of study. A promising candidate is feedback from energy injection by the central AGN of the cD galaxy (e.g., Churazov et al. 2001; Churazov et al. 2002; for a review see McNamara & Nulsen 2007). However, the details of this interaction, and how the energy is transferred from the jets to the ambient ICM, are poorly understood. Galaxy groups provide an excellent opportunity to study heating and other non-gravitational processes in the ICM. Although

not as X-ray luminous as clusters, the effects of heating are more readily apparent in groups, due to their lower gas temperatures, masses, and central densities. For example, the gas to total mass fraction in groups ranges from 0.02–0.07, with a scatter of ~ 2 at a fixed temperature within r_{2500} . The scatter is tightly correlated with the central entropy (Gastaldello et al. 2007; Sun et al. 2009), reflecting the greater role of non-gravitational processes in the centers of groups as compared to clusters.

In this paper, we report on *Chandra* observations of NGC 5813 (UGC 09655), a bright ($M_V = -22.01$, Lauer et al. 2007) E1 galaxy. It is the central dominant member of a subgroup (which we shall call the NGC 5813 galaxy group) in the NGC 5846 galaxy group (Mahdavi et al. 2005). NGC 5846 and NGC 5813 have a projected separation of 79.7' (740 kpc). This group is relatively isolated, lying well off the plane of the Local Supercluster. Both the NGC 5813 and NGC 5846 galaxy groups are members of the *ROSAT*-ESO Flux-Limited X-ray (REFLEX) galaxy cluster catalog (Böhringer et al. 2004). Detailed *Hubble Space Telescope* (*HST*) observations reveal that NGC 5813 contains a relatively undisturbed dusty circumnuclear disk (Tran et al. 2001), suggesting that this galaxy has not recently experienced a major merger. Emsellem et al. (2007) classify NGC 5813 as a “slow rotator” galaxy which, they argue, represents the extreme evolutionary end point reached in deep potential wells, consistent with this object being a dynamically old galaxy at the center of a galaxy subgroup. NGC 5813 contains a $2.8 \times 10^8 M_\odot$ supermassive black

¹ Harvard-Smithsonian Center for Astrophysics, 60 Garden St., Cambridge, MA 02138, USA; srrandall@cfa.harvard.edu

² INAF/IRA, via Gobetti 101, I-40129 Bologna, Italy

³ Department of Astronomy, University of Virginia, P.O. Box 400325, Charlottesville, VA 22901, USA

⁴ Max-Planck-Institut für Astrophysik, Karl-Schwarzschild-Strasse 1, 85741 Garching, Germany

⁵ Space Research Institute (IKI), Profsoyuznaya 84/32, Moscow 117810, Russia

⁶ Physics & Astronomy Department, Michigan State University, East Lansing, MI 48824-2320, USA

⁷ Institute for Astrophysical Research and Astronomy Department, Boston University, 725 Commonwealth Avenue, Boston, MA 02215, USA

⁸ KIPAC, Stanford University, 452 Lomita Mall, Stanford, CA 94305, USA

hole (SMBH), and an associated AGN that is a known radio source (e.g., Balmaverde & Capetti 2006; Magliocchetti & Brüggen 2007).

We report here on a 150 ksec combined observation of NGC 5813 with the *Chandra X-ray Observatory*, an analysis of archival multi-frequency *Very Large Array* (VLA) observations, H α observations with the *Southern Astrophysics Research Telescope* (SOAR), and on some initial results from low frequency *Giant Metrewave Radio Telescope* (GMRT) radio observations. We focus on three main results:

1. The ICM in NGC 5813 shows clear signatures from three distinct AGN outbursts, with three pairs of roughly collinear cavities and unambiguous shocks with measured temperature jumps associated with the inner and intermediate cavities.
2. The mean power of the two most recent outbursts differs by a factor of six, from $1.5\text{--}10 \times 10^{42} \text{ erg s}^{-1}$, even in this otherwise dynamically relaxed system, indicating that the mean jet power varies over long ($\sim 10^7 \text{ yr}$) timescales.
3. The heating from shocks alone is sufficient to offset radiative cooling locally (within at least 10 kpc), without requiring the internal energy of the X-ray cavities. The heating is roughly isotropic, and strongest near the AGN where the shock Mach numbers are larger, which is the region of interest for regulating feedback between the ICM and the central SMBH.

We assume an angular diameter distance to NGC 5813 of 32.2 Mpc (Tonry et al. 2001), which gives a scale of 0.15 kpc/" for $\Omega_0 = 0.3$, $\Omega_\Lambda = 0.7$, and $H_0 = 70 \text{ km s}^{-1} \text{ Mpc}^{-1}$. All uncertainty ranges are 68% confidence intervals (i.e., 1σ), unless otherwise stated.

2. OBSERVATIONS AND DATA REDUCTION

2.1. Chandra Observations

NGC 5813 was originally observed with *Chandra* on April 2, 2005, for 49 ksec (ObsID 5907) with the *Chandra* CCD Imaging Spectrometer (ACIS), pointed such that the galaxy was centered on the back-side illuminated ACIS-S3 CCD (the ACIS-S1 as well as the front-side illuminated ACIS-I3 and ACIS-S2 CCDs were also active). It was subsequently observed for 100 ksec on June 5, 2008 (ObsID 9517) with the same chip configuration. These data were reduced using the method described in Randall et al. (2008). All data were reprocessed from the level 1 event files using the latest calibration files (as of CIAO4.2). CTI and time-dependent gain corrections were applied. LC_CLEAN was used to remove background flares⁹. The mean event rate was calculated from a source free region using time bins within 3σ of the overall mean, and bins outside a factor of 1.2 of this mean were discarded. There were no periods of strong background flares. The resulting cleaned exposure times were 48.7 and 99.6 ksec, respectively.

Diffuse emission from NGC 5813 fills the image FOV for each observation. We therefore used the CALDB¹⁰

blank sky background files appropriate for each observation (including the new “period E” files for the more recent observation), normalized to our observations in the 10–12 keV energy band. To generate exposure maps, we used a MEKAL model with $kT = 0.7 \text{ keV}$, Galactic absorption, and abundance of 30% solar at a redshift $z = 0.006578$, which is consistent with typical results for the extended emission from detailed spectral fits (see § 4).

The exposure corrected, background subtracted, 0.3–2 keV *Chandra* image is shown in Figure 1. To enhance the visibility of the diffuse emission, bright point sources were removed, and the regions containing point sources were “filled in” using a Poisson distribution whose mean was equal to that of a local annular background region. A close-up of the core in Figure 2 shows small-scale structure in the center, while the more heavily smoothed image in Figure 3 shows structure in the fainter outer regions. We discuss the main features in these images in § 3.

All X-ray spectra were fitted in the 0.6–3.0 keV band and grouped to a minimum of 40 counts per spectral bin. The absorption was fixed to the Galactic value of $N_H = 4.37 \times 10^{20} \text{ cm}^{-2}$ (Kalberla et al. 2005). Varying the absorption from the Galactic value did not significantly improve the fit. Anders & Grevesse (1989) abundance ratios were assumed throughout, unless otherwise stated. Temperature maps were derived using the method of Randall et al. (2008). For each temperature map pixel, we extracted a spectrum from a circular region containing a minimum number of net counts (after subtracting the blank sky background) in the 0.6 – 3.0 keV band. The resulting spectrum was fitted with an absorbed APEC model using XSPEC, with the abundance allowed to vary.

2.2. Radio Observations

NGC 5813 was observed with the GMRT at 235 MHz, as part of a larger, ongoing project (Giacintucci et al. 2009; Giacintucci et al. 2010). The observations were carried out in August 2008 for a total of 100 minutes on source. The NRAO Astronomical Image Processing System (AIPS) package was used for the data reduction and analysis. The visibilities were inspected and edited to identify and remove bad data. After the initial calibration, phase-only self-calibration was applied to remove residual phase variations. Multi-field imaging was implemented in each step of the data reduction. The rms noise level (1σ) achieved in the image is 0.3 mJy/beam. We refer to Giacintucci et al. (2010) for a detailed description of the data reduction and analysis.

We also include results from an analysis of archival VLA observations at multiple frequencies. Data calibration and imaging were carried out in AIPS following the standard procedure (Fourier-transform, Clean and Restore). Phase-only self-calibration was applied to remove residual phase variations and improve the quality of the image. The properties of the VLA and GMRT radio observations are summarized in Table 1.

2.3. H α Observations

Narrow-band H α imaging observations were made with the SOAR Optical Imager (SOI) on July 6, 2008 (UT).

⁹ <http://asc.harvard.edu/contrib/maxim/acisbg/>

¹⁰ <http://cxc.harvard.edu/caldb/>

The night was clear and photometric. Two CTIO narrow-band filters were used, 660075-4 for the H α + [NII] lines and 6129/140 for the continuum. Three 15-minute exposures were taken with the 660075-4 filter and three 12-minute exposures were taken with the 6129/140 filter. Spectroscopic standard stars were EG274 and LTT7987. More detail on the SOI data reduction can be found in Sun et al. (2007).

3. X-RAY CAVITIES AND SHOCKS

As we discuss in detail in this paper, the X-ray images show signatures from three episodes of AGN activity. There are two clear pairs of cavities distributed collinearly (in a direction roughly parallel to the minor axis of the elliptical optical isophotes) and symmetrically about the galaxy center, each pair associated with a shock. In addition, we argue for a third pair of cavities at larger radii (along roughly the same line) and an associated third surface brightness edge, which may be a weak shock. In detail, we see the following:

1. A pair of inner cavities at ~ 1.4 kpc, inflated by the most recent AGN outburst about 3×10^6 yr ago (Figure 2). The cavities are surrounded by bright rims of emission, similar to what is seen in other systems (e.g., the Perseus Cluster Fabian et al. 2003, M87 Forman et al. 2007; M84 Finoguenov et al. 2008, Abell 2052 Blanton et al. 2009; see Figure 2), though here we find the rims to be hotter than the ambient gas, whereas in other systems they are typically cooler. We identify the sharp edge in the rims, 1.4 kpc southeast of the AGN, as a shock, which we refer to as the 1.5 kpc shock, with a Mach number of $M = 1.7$ (see § 5.1). The rims overlap to form an indented structure to the northwest. The northeastern inner cavity has an irregular morphology, possibly due to the wall of the cavity being “punched through” by the AGN jet.
2. A pair of intermediate cavities at ~ 8 kpc, inflated by a previous AGN outburst about 2×10^7 yr ago (Figure 1, Figure 4). The southwestern cavity has a regular morphology, while the northeastern cavity is more extended in the radial direction and may be a double “Russian doll” cavity (e.g., as in M84, Finoguenov et al. 2008). The intermediate cavities lie just inside a sharp, elliptical edge, which we identify as a shock (and refer to as the 10 kpc shock) with $M = 1.5$ (see § 5.1).
3. A faint pair of outer cavities, at ~ 20 kpc, inflated by a previous outburst about 9×10^7 yr ago (Figure 3, Figure 4). The northeastern outer cavity is surrounded by a rim of brighter emission, while the southwestern outer cavity is a weaker feature (see § 5.3). The outer cavities are associated with a weak outer edge-like feature at ~ 25 kpc (Figure 3), just past the outer edges of the cavities. This feature may represent an old shock, or a transition region from the galaxy atmosphere to the extended group atmosphere (see § 5.2).
4. A central point source, offset ~ 0.5 kpc southeast of the axis defined by the cavities (Figure 2), with an

X-ray luminosity of $L_X = 1.6 \times 10^{39}$ erg s $^{-1}$ in the 0.3 – 12.0 keV rest frame energy band. Although this source is quite faint, we identify it as the AGN that has inflated the X-ray cavities and driven the shocks in the ICM due to its central location and detection in the radio (see § 4.2.5)

Since it is difficult to show all the cavities simultaneously in the same image, we divided the X-ray image by a β -model to better show surface brightness fluctuations over a wider dynamic range. The resulting image is shown in Figure 4, with the cavities indicated by overlaid regions for clarity. The overall morphology of NGC 5813 is remarkably symmetric and regular, suggesting that AGN feedback maintains a near “steady state” through regular outbursts in an otherwise undisturbed system (consistent with optical studies that also conclude NGC 5813 is dynamically old, Tran et al. 2001; Emsellem et al. 2007).

3.1. Radio Emission from the X-ray Cavities

Radio contours from our 235 MHz *GMRT* observations (green) and archival 1.36 GHz *VLA* observations (blue) are shown overlaid on the *Chandra* image of the core in Figure 5. Extended radio emission at 1.36 GHz fills the inner cavities, while the 235 MHz emission overfills the cavities, extending along the axis of symmetry of the cavities (this extension is real, and not due to the larger beam size at 235 MHz). The intermediate cavities are filled with 235 MHz radio emission, but show no emission at 1.36 GHz. The intermediate cavities are also not detected at 1.4 GHz in the *NRAO VLA Sky Survey* (NVSS, which has a beam size of 45”) or at 1.36 GHz in archival *VLA* C array configuration observations (see Table 1). The outer cavities, which are outside the FOV of Figure 5, do not show any detected radio emission. The radio images are therefore qualitatively consistent with what is expected for intermittent AGN outbursts, where the electrons contained in the cavities age due to synchrotron, inverse Compton, and adiabatic losses as the cavities rise buoyantly after the outburst phase. The central cavities contain recently accelerated electrons, which emit at high and low frequencies, while older cavities contain older electron populations with fewer energetic particles and weaker high frequency emission.

4. THE THERMAL STRUCTURE OF THE GAS

4.1. Temperature Map

The X-ray image (Figure 1) shows complicated structure in the ICM, which fills the FOV. To study the thermal structure of the ICM, we generated a temperature map, requiring 1500 net counts per extraction region. The resulting temperature map, with the X-ray cavity regions overlaid, is shown in Figure 6. The corresponding pseudo-pressure and pseudo-entropy maps are shown in Figure 7. The extraction radii range from 2.8” (0.4 kpc) in bright regions near the core to 59” (9 kpc) in faint outer regions. The temperature uncertainties are between 2% – 3% across the map.

The temperature map shows that even in the projected, effectively smoothed map, the hot (0.7–0.75 keV) 10 kpc shocks are visible at the location of the prominent surface brightness edges. The pseudo-pressure map also shows large jumps across the edges, consistent with

these features being shock fronts. There is a trail of cool 0.55 keV gas through the galaxy center, along the line defined by the X-ray cavities indicated in Figure 1, terminating at the edges of the intermediate cavities (we discuss this feature further in § 5.4). The $kT \sim 0.65$ keV gas extends to larger radii (out to ~ 27 kpc) in the east-northeast, coincident with the extension of diffuse emission across the outer edge in Figure 3. East of this extension, the temperature rises rapidly from about 0.65 keV to 0.75 keV over ~ 7 kpc.

To study the detailed structure in the core, we made a higher angular resolution temperature map of the central region of NGC 5813. In addition to the finer spatial binning, each extracted spectrum had only 1000 net counts, giving smaller extraction radii (and thus less smoothing in the map), ranging from 0.4 kpc to 1.8 kpc. The resulting temperature map is shown in Figure 8, and the corresponding pressure and entropy maps in Figure 9, with the 0.3–2.0 keV X-ray surface brightness contours overlaid. The bright rims surrounding the innermost bubbles are revealed to contain relatively hot ($kT \approx 0.7$ keV), high pressure gas, in contrast to the cool bubble rims seen in some other systems (e.g., the Perseus Cluster, Fabian et al. 2003; M87, Forman et al. 2007; Abell 2052, Blanton et al. 2009). The gas in the rims has likely been shock heated by a recent AGN outburst, which has rapidly inflated the innermost cavities.

4.2. Detailed Spectral Analysis

4.2.1. Azimuthally Averaged Profiles

We produced projected radial profiles by fitting spectra extracted from concentric annuli, centered on the centroid of the diffuse emission at larger radii. Each annular bin was fitted with an absorbed APEC model, with the abundance allowed to vary. The resulting temperature profile is shown in the top panel of Figure 10. There is a temperature increase of ~ 0.05 keV at ~ 10 kpc, at the location of the surface brightness edges indicated in Figure 1, unambiguously identifying these features as shocks. Additionally, there is an inner temperature jump of ~ 0.06 keV at ~ 2 kpc, at the location of the bright rims around the inner bubbles, consistent with the core temperature map shown in Figure 8. Although the point source presumed to be the central AGN has been excluded, the temperature profile shows a strong central spike. This is because the profile center is in the region of the hot overlapping rims of the central cavities, shown in Figure 2.

4.2.2. Deprojection Analysis

To determine the 3D structure of the ICM we performed a deprojection analysis using concentric annuli as in § 4.2.1, but with bins 2–3 times larger to provide adequate statistics for the deprojection analysis. We used the “onion peeling” method (employed, e.g., by Fabian et al. 1981, Blanton et al. 2003) to derive deprojected profiles. First, the projected temperature, abundance, and XSPEC normalization are determined by fitting an absorbed APEC model to the outermost annulus. Fits to spectra from annuli at smaller radii are then determined by adding an additional component for each outer annulus, with fixed temperature and abundance, and a normalization scaled to project from the outer to the inner

annulus, assuming spherical symmetry. We note that this procedure does not correctly account for the uncertainties, since the contributions from outer shells are fixed. This method was adopted instead of simultaneously fitting spectra in all of the bins (e.g., with the PROJCT model in XSPEC) to prevent spectra at small radii, where the spherical symmetry approximation is less accurate, influencing the fitting results at large radii. A comparison of the two methods shows that while the best-fitting temperature profile is not significantly affected, the density profile determined with the PROJCT model differs somewhat from the profile we present here and shows a $\sim 50\%$ increase in density with radius between 6–9 kpc (in the region of the intermediate bubbles and 10 kpc shock front). Thus, while the azimuthally averaged deprojected temperature profile is not significantly affected by the assumption of spherical symmetry, the density profile is sensitive to this assumption and is therefore only approximate.

As a further check on the deprojection, we performed an independent analysis, with the data analyzed as described in Vikhlinin et al. (2005) and the deprojection method described in Churazov et al. (2008, 2010). This method accounts for emission at large radii by assuming a power law density profile for emission outside of the FOV and fitting the normalization of this component along with the fluxes from spherical shells. The derived temperatures agreed within the 1σ confidence range, and the temperature jumps were fully consistent within the uncertainties.

In the case of NGC 5813, measuring the deprojected abundance profile is extremely difficult. This is because at these relatively low gas temperatures (0.6–0.7 keV) the spectral resolution of the ACIS instrument is such that there is a strong degeneracy between line emission (which determines the abundance) and continuum emission (which determines the electron density). When this effect is accumulated across several shells and projected onto the inner shells, the inner abundances are essentially indeterminate, leading to a highly uncertain density profile. Furthermore, determining abundances in multiphase gas is a known problem (e.g., Buote 1999; Rasia et al. 2008). We therefore fixed the abundance at 50% solar, which is an average value from the projected profile fits.

The resulting deprojected (red triangles) and projected (black circles) temperature profiles are shown in the top panel of Figure 10, alongside the corresponding density, pressure, and entropy profiles. The entropy is taken to be $S = kTn_e^{-2/3}$ and the pressure $P = nkT$, where n_e is the electron density and $n = 1.8n_e$. The most significant effect of the deprojection on the temperature profile is the lower temperature of the gas at ~ 5 kpc (0.55 keV versus 0.61 keV) once the projection effects from the outer shock-heated gas have been removed, as well as a significant increase in the central temperature (from 0.65 keV to 0.7 keV). Note that in these plots the shock front edges are smeared over multiple bins since they are not spherically symmetric with respect to the galaxy center.

4.2.3. Temperature Profile Across the Shocks

The azimuthally averaged temperature profiles (Figure 10) and projected temperature (Figure 6) map show temperature rises at the location of the surface bright-

ness edges, characteristic of shock fronts. We therefore extracted spectra in sectors across these edges to better characterize the temperature jumps. Each sector was centered on the center of curvature defined by the corresponding edge, which is *not* coincident with the central position used to extract the azimuthally averaged profiles. The extraction regions were truncated at small radii to avoid the complex structure in the central region (additionally, the assumption of spherical symmetry breaks down at small radii since the centers of curvature are not coincident with the overall centroid of the diffuse emission). The projected and deprojected temperature profiles are shown in Figure 11. The northwestern region shows higher overall temperatures and a larger temperature jump of ~ 0.15 keV as compared to ~ 0.1 keV in the southeast (where we estimate the size of the jumps by extrapolating the base-line deprojected temperature increase on either side of the temperature peak, roughly from $r < 10$ kpc and $r > 18$ kpc). The lower temperatures in the southeast are likely due in part to the east-northeast extension of cool gas seen in the temperature map (§ 4.1), which overlaps with the extraction annuli.

4.2.4. Total Diffuse Emission

To accurately determine the weighted average properties of the diffuse gas, we extracted and fitted spectra for the total diffuse emission within $2.9'$ (27 kpc). We initially fitted the spectra with a single APEC model. The resulting model showed residuals near the 1.8 keV Si and 2.46 keV S lines, possibly indicating non-solar abundance ratios. We therefore fit the spectra with a VAPEC model with the abundances of O, Ne, Mg, Si, S, and Fe allowed to vary independently (other elements were not well constrained and were fixed at $1/2$ the solar abundance, except He which was fixed at solar). The resulting fitted abundance values were 0.8 – 1.0 solar, with Si and S having somewhat larger values than Ne and Mg, except for O ($Z_O = 0.35 \pm 0.03$) and Fe ($Z_{Fe} = 0.65 \pm 0.03$). Since the total diffuse emission is expected to include emission from gas at multiple temperatures, we added a second VAPEC component to the model and tied individual abundances for the two components together. This model provided a much improved fit, with abundance values of $Z_O = 0.13^{+0.03}_{-0.02}$, $Z_{Ne} = 0.59^{+0.05}_{-0.04}$, $Z_{Mg} = 0.65 \pm 0.04$, $Z_{Si} = 0.78 \pm 0.04$, $Z_S = 0.94 \pm 0.08$, and $Z_{Fe} = 0.53 \pm 0.03$. The fitted temperatures were $kT_1 = 0.35^{+0.03}_{-0.01}$ and $kT_2 = 0.671^{+0.011}_{-0.007}$. We tried including a power-law component in each of the above models, but in no case did this addition improve the fit (even if the photon index was fixed at a typical value of 1.5 for an unresolved LMXBs population) or tightly constrain the photon index. This suggests that emission from unresolved LMXBs is not significant in this energy band. We note that the above results depend somewhat on the adopted abundance table. If we adopt the updated abundance table of Grevesse & Sauval (1998), we find that Fe is no longer under-abundant compared to the other elements, with Z_{Fe} , Z_S , and Z_{Si} all roughly 0.7 solar, and Z_{Ne} and Z_{Mg} about 0.6 solar. O is still found to be under-abundant, with $Z_O = 0.16^{+0.04}_{-0.03}$. This difference in the fitted value for Z_{Fe} was noted previously, e.g., by Humphrey et al. (2004).

As a further check of this result, we examined data

from *XMM-Newton* RGS observations, which has better spectral resolution in the region of the O lines. The processing of the RGS data is described in Werner et al. (2009). We fitted the spectrum from a $1'$ wide region centered on the core of NGC 5813 between 10–25 Å with a collisionally ionized plasma (CIE) model with two cooling flow components, one to account for gas cooling down to 0.4 keV and a second to account for gas cooling to lower temperatures. The abundances were constrained to be equal across each model component. We found best-fitting abundance values of $Z_{Fe} = 0.60 \pm 0.06$, $Z_O = 0.44 \pm 0.06$, and $Z_{Ne} = 0.42 \pm 0.06$. Although this gives a higher Z_O/Z_{Fe} ratio (0.7 versus 0.2 from *Chandra*), O is still found to be under-abundant as compared to Fe. We conclude that there is evidence for non-solar abundance ratios in the diffuse ICM, with the most robust result being a decreased O abundance relative to solar. Similar sub-solar values for Z_O/Z_{Fe} have been reported for other galaxy groups, massive elliptical galaxies, and clusters of galaxies, and imply a greater relative enrichment from Type Ia supernovae as compared to Type II (e.g., Finoguenov et al. 2000; Finoguenov et al. 2001). However, sub-solar Z_O/Z_{Fe} values are difficult to reconcile with the larger Z_{Si}/Z_{Fe} and Z_S/Z_{Fe} abundance ratios when one tries to apply SN enrichment models to explain the observed ICM abundances (see Humphrey et al. 2004 and references therein for a discussion).

4.2.5. The Central Source

NGC 5813 contains a central X-ray point source, visible in Figure 2. We extracted a spectrum for the central source using an aperture with a radius of $1.5''$ and a background determined from a local annular region. The spectrum, which had 550 counts in the 0.6–5.0 keV band, was fitted with an absorbed power-law, giving a best-fitting photon index of $\Gamma = 1.5^{+0.5}_{-0.6}$. The nuclear X-ray luminosity is $L_X = 1.6^{+0.8}_{-0.5} \times 10^{39}$ erg s $^{-1}$ in the 0.3 – 12.0 keV rest frame energy band (90% confidence ranges). We calculated the radio luminosity between 10 MHz and 100 GHz using archival VLA A array configuration observations of the core at 1.49 GHz and 4.86 GHz. This gave a spectral index of $\alpha_r = 0.35$ and a luminosity of $L_R = 1 \times 10^{36}$ erg s $^{-1}$. Even though the spectral index indicates a relatively flat spectrum for a core AGN, giving a larger estimate of the broad band luminosity than would a steeper spectrum, the calculated luminosity is still two orders of magnitude fainter than the faintest source in the sample of systems containing X-ray cavities given in Birzan et al. (2008). However, they mainly consider sources at the cores of galaxy clusters, which are higher mass systems than the subgroup we consider here.

Although the central source is X-ray faint enough to be classified as an ultraluminous X-ray source (ULX), we identify it as the AGN that has inflated the X-ray cavities and driven the shocks in the ICM due to its central location and detection in the radio (see Figure 5). Its low luminosity identifies this source as a low luminosity AGN, which typically have $L_X < 1 \times 10^{42}$ erg s $^{-1}$ (Ptak 2001). This suggests that the source is either faint yet mechanically powerful, in a quiescent state after having recently had an outburst that inflated the inner X-ray

cavities, or heavily obscured (allowing the absorption to vary gave a value that was 4 times Galactic, although the fit was not improved and the absorption was consistent with the Galactic value to within 1σ).

5. DISCUSSION

5.1. Structure of the Shock Fronts

The hard band image, temperature and pressure maps, and deprojected temperature and pressure profiles identify the prominent surface brightness edges around the intermediate cavities as shock fronts. To quantitatively study the structure of these shocks, we extracted the 0.3–2.0 keV surface brightness profiles from the sectors used to derive the temperature profiles shown in Figure 11. Note that the profiles are defined by the centers of curvature of the 10 kpc shocks, which do *not* coincide with the location of the central AGN. The profiles were then converted to integrated emission measure (IEM) profiles, using the temperatures from the projected temperature profile shown in Figure 11, with the abundance fixed at 50% solar (roughly the average from projected profile fits in this region, see § 4.2.2). The resulting IEM profiles are shown in Figure 12. Each profile shows a sharp edge at ~ 13 kpc. Following our previous work (Vikhlinin et al. 2001; Randall et al. 2009a, 2009b), we fit the profiles by projecting a 3 dimensional density profile consisting of two power laws, connected by a discontinuous break, or “jump”. The free parameters were the normalization, the inner (α) and outer (β) power law slopes, the position of the density discontinuity (b_{break}), and the amplitude of the jump (A). The best-fitting model is shown as the solid lines in Figure 12, with the fitted break radii indicated by the vertical dashed lines. The best fitting inner density jumps for the northwest and southeast sectors are $A_{\text{nw}} = 1.75^{+0.04}_{-0.03}$ and $A_{\text{se}} = 1.69 \pm 0.07$. Using the Rankine-Hugoniot shock jump conditions for a $\gamma = 5/3$ gas implies Mach numbers of $M_{\text{nw}} = 1.53$ and $M_{\text{se}} = 1.48$, and temperature jumps by the same factor as the Mach numbers. The predicted temperature jumps are greater than the temperature jumps of ~ 1.2 detected in the deprojected temperature profiles (Figure 11). We discuss this discrepancy below.

The core temperature map (Figure 8) and the azimuthally averaged temperature profile (Figure 10) show evidence for shock heated gas in the bright rims surrounding the innermost bubbles, about 1 – 2 kpc from the central AGN. The X-ray image of the core (Figure 2) shows a sharp contrast between the bright bubble rims and the surrounding gas, with the sharpest edge to the southeast. We extracted the surface brightness profile in a 52° wide sector across the southeastern edge, centered on the AGN, and fit the IEM profile with a broken power law density model as above. To the northwest, the morphology is more complicated, with the two rims meeting to form an indented structure. Since this structure is not well-modeled by our assumption of spherical symmetry we did not fit the IEM profile to the northwest. There were too few counts to accurately measure the temperature profile across the southeast, so we assumed an isothermal gas with $kT = 0.6$ keV and 50% solar abundance. The resulting IEM profile, along with the best fitting model, is shown in Figure 13. The deviant point at 2 kpc is due to small-scale clumpiness in the

ICM, visible in the X-ray image. We find a density jump of 1.97 ± 0.12 , which corresponds to a $M = 1.71 \pm 0.1$ shock with a temperature jump of 1.72 ± 0.12 . Unfortunately, there are too few counts to derive a deprojected temperature profile to compare to the inferred temperature jump, although the corresponding inner jump in the azimuthally averaged temperature profile of about 1.1 (Figure 10) is much smaller than the jump of 1.7 predicted from the density discontinuity. To better quantify the temperature jump across the 1.5 kpc shock, we extracted a spectrum of the total emission from the post-shock region in the core wedge used to fit the surface brightness profile, and from a similar sized region in the same wedge just outside the shock edge. We find that the (inner) post-shock region is best fit by a two temperature thermal model, with best-fitting temperatures of $kT_1 = 0.64^{+0.03}_{-0.04}$ and $kT_2 = 0.97^{+0.21}_{-0.17}$, while the pre-shock region is adequately described by a single thermal model with $kT = 0.5 \pm 0.01$. If we assume that the two thermal components in the post-shock region give the temperatures of the shocked gas and local projected pre-shocked gas this gives a temperature jump of 1.5 ± 0.3 . This is consistent with a temperature jump of 1.7 as expected from the Mach number, although the large uncertainties limit the usefulness of this comparison. The properties of the 10 kpc and 1.5 kpc shocks are summarized in Table 2.

For both the 1.5 kpc and 10 kpc shocks, the observed temperature rise is less than what is expected based on the Mach number, even in the deprojected temperature profiles. To better estimate the expected measured temperature rise associated with the shocks we ran 1D hydrodynamical simulations to fully model their evolution. For the 10 kpc shocks, the simulations start with an isothermal sphere with $kT = 0.67$ and a power law density profile, in hydrostatic equilibrium. The logarithmic slope of the density profile was taken to be 1.46, which was determined by fitting the slope of the surface brightness profile beyond the 10 kpc shocks. The shocks were initiated by a central point explosion and allowed to propagate freely. Since the gas is initially isothermal with a power law density profile, the simulations are scale free, so we can choose the point of evolution at which the code best reproduces the observed surface brightness jump at the shock front and scale accordingly. The resulting Mach number for the 10 kpc shocks is $M = 1.52$, in excellent agreement with what was found above by fitting a discontinuous power law density model to the integrated emission measure profile. The expected projected temperature profile is shown in Figure 14. The solid lines show the emission weighted temperature (with 90% confidence ranges) and the points show single temperature fits to more accurately simulated model spectra folded through the *Chandra* response (the discrepancy between emission weighted temperatures and fitted temperatures for multi-temperature gas has previously been noted by Mazzotta et al. 2004). The simulations predict a projected temperature rise of ~ 0.1 keV, consistent with observations (see Figure 10). Similar simulations fit to the 1.5 kpc shock to the southeast predict a measured projected temperature rise of $\sim 30\%$, consistent with observations (although the observational uncertainties are large). We conclude that the projected temperature profiles are consistent with the calculated Mach numbers (although the temperature

structure of the 1.5 kpc shock is poorly constrained). The deprojected temperature measurements cannot resolve the temperature jump due to the narrow width of the shock and the rarefied cool gas behind the shock (the temperature of which drops slightly below the ambient temperature in our isothermal simulations).

5.2. The Outer Edge at 25 kpc

There is a weak surface brightness edge (most clearly seen in Figure 3) surrounding most of NGC 5813 at a distance of $\sim 160''$ (25 kpc) from the central AGN. To check the significance of this feature we extracted the surface brightness profile across this edge in two sectors, one to the northwest between 12° - 79° (measured north from west, the same angular range spanned by the bright section of the elliptical edge to the northwest) and a wider wedge between 206° - 320° to the south. The wedges were chosen to match the curvature of the outer edge, so that the profiles were off center from the peak of the overall diffuse emission. The resulting surface brightness profiles are shown in Figure 15. Both profiles show a similar change in slope at $\sim 170''$ (26 kpc), at the position of the outer edge, and the northwestern profile shows a sharp jump at the same location. We conclude that the outer edge-like feature indicated in Figure 3 is real, and corresponds to a change in slope and possibly a discontinuity in the surface brightness profile. The edge lies just beyond the outer X-ray cavities indicated in Figure 3, and the association is reminiscent of the 1.5 kpc and 10 kpc shocks to the inner and intermediate cavities. The discontinuous jump is also stronger in the northwest than in the south, consistent with what is seen for the elliptical 10 kpc shock front edge. It may therefore represent the weak remnants of a shock associated with this older outburst.

To determine the nature of this edge, we fit the surface brightness profile in the wedge to the the south, where this feature is the sharpest. Although there is a significant surface brightness discontinuity to the northwest (see Figure 15), we focus on the wedge to the south, since we have better statistics in the wider southern wedge, and since the shape of the northwestern discontinuity is not well-described by our shock model density profile (compare the profile shapes in Figure 15 and in Figure 12). The shape of the surface brightness profile is obviously not well-described by a single power-law, and modeling this profile with a projected power-law density model did not provide an acceptable fit. We also fit the profile with a β -model density profile, which gave a poor fit with $\chi^2_\nu = 13.9/6$. The fitted model showed asymmetric residuals in the region of the surface brightness edge, so we tried fitting the edge with a projected discontinuous power-law density model, as in § 5.1. This gave an improved fit, with $\chi^2_\nu = 0.4/4$, and a density jump factor of $A_{\text{outer}} = 1.06^{+0.12}_{-0.13}$, consistent with no jump. The inner and outer slopes of the density profile were $\alpha = -0.62^{+0.09}_{-0.18}$ and $\beta = -2.30^{+0.25}_{-0.32}$. Unfortunately, there were inadequate statistics to measure the temperature and abundance profiles across this outer edge and confirm it as an old shock. In particular, the edge could in principle be a metallicity edge, or the interface between the galaxy atmosphere and the extended group atmosphere (where one would expect to see a change in

slope of the surface brightness profile). We conclude that, while the outer edge is consistent with an old shock with $M \approx 1.1$ associated with the outermost X-ray cavities, the data are also consistent with no density jump and further observations are needed to determine its nature.

5.3. The X-ray Cavities

The X-ray image shows three pairs of roughly collinear cavities (Figure 1, Figure 4). Although most of the cavities are clear, the outermost cavities (in particular, the southwestern outer cavity) are weak features. To check their significance, we extracted surface brightness profiles across each outer cavity, centered on the overall diffuse emission. The resulting profiles are shown in Figure 16. Each profile shows a significant dip at the location of the outer cavities. The profile across the northeastern cavity also shows a significant hump just beyond the cavity dip, corresponding to the bright outer rim seen in the X-ray images. For the southwestern outer cavity, the rise just outside the cavity is less pronounced, since it lacks a bright rim. We conclude that the faint outer southwestern cavity indicated in Figure 3 is likely a real feature and represents a paired cavity to the outer northeastern cavity, each initially created by the same AGN outburst from the central SMBH.

Each of the three pairs of X-ray cavities in NGC 5813 is likely associated with a distinct AGN outburst. Although the position angle of the inner and intermediate cavity pairs appears to vary slightly, by about 10° - 15° , possibly indicating that the central black hole that has inflated the cavities is precessing, the cavities are roughly collinear. The fact that the cavities are regular and collinear suggest that they have evolved passively, i.e., have not been disturbed by gas motions due to sloshing, turbulence, mergers, etc., consistent with previous conclusions on the dynamical state of this system (Tran et al. 2001; Emsellem et al. 2007). Measuring the properties of these cavities is therefore of great interest, since a comparison of the different pairs will provide information on how the cavities evolve, and on the outburst history of the central AGN (in particular, we want to know whether the outbursts have a similar total energy output and mean power, as might be expected in a near “steady state” AGN feedback model, or whether the outbursts change significantly even in an otherwise apparently relaxed system like NGC 5813).

5.3.1. Cavity Ages and Energies

Table 3 summarizes the properties of the X-ray cavities, which are shown as overlaid regions in Figure 4. We assume that the cavities rise in the plane of the sky, that the mass of material within the cavities is negligible, and that each cavity has a spherical or oblate spheroidal geometry with the minor axis in the plane of the sky. The former assumption is suggested by the fact that the cavities are detected in the image, and that the inner two pairs are near the same projected radii as their associated shock fronts. If the global gas distribution was significantly extended along the line of sight, with the bubbles rising along this extension, they would be difficult to detect for large inclination angles of the extension due to the large column of cool gas at smaller radii behind (or in front of) the bubbles (see Bîrzan et al. 2009).

Columns 2 & 3 in Table 3 give the cavity major and minor axis, respectively, and Column 4 gives the distance from the AGN to the center of the cavity. The rise time of the cavities, given in Column 5, is calculated assuming that they rise buoyantly at half the sound speed c_s , similar to what is found from simulations (e.g., $0.6\text{--}0.7c_s$ in Churazov et al. 2001). For a $kT = 0.65$ keV gas, the sound speed is $c_s = 416 \text{ km s}^{-1}$. Note that for the innermost cavities, the distance from the AGN is comparable to the cavity size, suggesting that they are currently being, or have only recently been, inflated by the AGN. Therefore the rise times, which are computed using the distance from the AGN to the cavity center, are not a reliable estimate of the true age, since early on the cavities are driven by the momentum of the jet (see Birzan et al. 2008).

Finally, the mechanical energy required to inflate the bubbles is given in Column 6, which we estimate as PV , where P is the pressure at the location of the bubble center (taken from the azimuthally averaged pressure profile shown in Figure 10) and V is the cavity volume. The total internal energy of each cavity is expected to be a few times the mechanical energy ($\sim 3PV$ for a relativistic plasma, see McNamara & Nulsen 2007).

The total mechanical energy is about the same for the southwestern and northeastern cavities for both the innermost ($\sim 1.3 \times 10^{55}$ erg) and intermediate ($\sim 1.4 \times 10^{56}$ erg) pairs (taking the sum of the two intermediate cavities to the northeast), consistent with each pair having formed in two distinct AGN outbursts. The mechanical energies for the outer cavities differ significantly from one another (2.6×10^{56} erg versus 6.0×10^{55} erg for the northeastern and southwestern cavities, respectively). We suggest three possibilities to explain this discrepancy. First, the outer southwestern cavity is only marginally detected, so its measured properties may be inaccurate. Second, the outer cavities may be in the process of breaking apart, as suggested by their significantly different volumes, and if they are not devoid of X-ray emitting gas, then the mechanical energy will be incorrectly estimated. Finally, Figure 1 shows that the intermediate northeastern cavities may connect to the outer northeastern cavity. If this is indeed the case, energy may “leak” from the intermediate to the outer cavity, adding to its internal energy and inflating it, making it easier to detect (there is no such connection in the southwest).

A comparison of the ages of the cavities (approximated by the rise times given in Table 3) and the shocks (approximated by the travel time given in Table 2) for the “inner” and “middle” features shows that they are similar ($\sim 10^7$ yr), consistent with the interpretation that each set of features was formed at the same time by the same outburst event. The cavity ages are systematically larger than the shock ages derived from our hydrodynamical simulations (by about a factor of 3). This is likely due to the cavities being initially driven and inflated at some significant distance from the central AGN, only to rise buoyantly after the end of the outburst, so that regarding the cavities as buoyantly rising bubbles early in their lives is not accurate. Thus, using the buoyant rise velocities of the cavities likely overestimates their ages.

5.3.2. Pressure Balance with the ICM

The non-thermal radio pressure in X-ray cavities, under the assumptions of hydrostatic equilibrium and electron dominated pressure, is commonly found to be less than the pressure of the surrounding gas derived from X-ray observations (Birzan et al. 2008). To accurately estimate the radio pressure, flux measurements at multiple frequencies are required to estimate the spectral index α_r of the radio emission. In NGC 5813, only the innermost cavities are detected at more than one frequency (see § 3.1). Unfortunately, the large beam size and contamination from extended emission outside the cavities at 235 MHz make it difficult to accurately measure α_r . Comparing the total emission in the region of the inner cavities, including contributions from extended emission outside of the central cavities at 235 MHz and 1.36 GHz (the latter detected in archival VLA C array configuration observations) and emission from the core, gives $\alpha_r = 0.88$. If we assume $\alpha_r = 0.7$ within the inner cavities, a typical value for young radio lobes (Birzan et al. 2008), we find that the non-thermal pressure in each cavity is $P_{rad} \sim 2.3 \times 10^{-12} \text{ erg cm}^{-3}$ (where we have used the revised equipartition equations of Brunetti et al. 1997 with a low-energy cut-off of $\gamma_{min} = 100$). This is much less than the X-ray gas pressure outside the cavities $P_{gas} \sim 10^{-10} \text{ erg cm}^{-3}$ (see Figure 10). Balancing the pressure with low energy electrons alone would require $\alpha_r \approx 2$, which is unusually steep for young radio cavities (Birzan et al. 2008). If we assume $\alpha_r = 0.7$ and vary the ratio of the energy in protons to the energy in electrons k , we find that $k \approx 2000$ is required to balance the non-thermal and X-ray gas pressures, which is typical for radio galaxies in cool cores (Birzan et al. 2008; Dunn et al. 2010; Gitti et al. 2010).

We compared the radio and cavity power of the inner cavities with predictions based on the Birzan et al. (2008) sample. The 1.36 GHz radio power for each of the inner cavities is $P_{1360} \approx 1 \times 10^{20} \text{ W Hz}^{-1}$. The relation of Birzan et al. (2008) then predicts a total cavity power of $P_{cav} \approx 9 \times 10^{42} \text{ erg s}^{-1}$. Taking the cavity ages and mechanical energy (PV) from Table 3 and assuming total cavity energies of $3PV$ gives a power of $P_{cav} \approx 4 \times 10^{41} \text{ erg s}^{-1}$ for the inner cavities, more than an order of magnitude less than the estimate from Birzan et al. (2008). However, it is within the range of the large scatter in the Birzan et al. (2008) sample (see their Figure 6). More recently, Cavagnolo et al. (2010) derive a relation between P_{cav} and P_{radio} for lower mass systems and find a steeper slope than Birzan et al. (2008). Their sample includes results from the *Chandra* observations of NGC 5813 we consider here, so that NGC 5813 is consistent with their derived relation.

5.4. Buoyantly Lifted Gas

The temperature map (Figure 6) shows an extension of cool gas along the line defined by the X-ray cavities, offset ~ 3 kpc to the southeast. This cool gas extends 11 kpc to the inner edges of the intermediate cavities. The most natural interpretation of this feature is cool gas that has been buoyantly lifted by the intermediate X-ray cavities, as seen in other systems (Forman et al. 2007; Simionescu et al. 2008; Kirkpatrick et al. 2009; Simionescu et al. 2009; Randall et al. 2010; Werner et al. 2010). The H α image, taken with the *SOAR* telescope

(Donahue et al. 2007), with the X-ray surface brightness contours overlaid, as well as the temperature map with the $H\alpha$ contours overlaid, are shown in Figure 17. The $H\alpha$ filaments are co-spatial with the trail of cool gas seen in the X-ray temperature map, as seen in many other systems (e.g., Sanders et al. 2007, 2009), confirming the presence of cool gas. Assuming line ratios of $N[\text{II}]\lambda 6583/H\alpha = 1$ and $N[\text{II}]\lambda 6548/H\alpha = 0.35$, the total $H\alpha$ flux is $F_{H\alpha} = 9.2 \times 10^{-14} \text{ erg s}^{-1} \text{ cm}^{-2}$ (assuming no intrinsic absorption). The Kennicutt relation for the star formation rate

$$\text{SFR}(M_{\odot}/\text{yr}) = 7.9 \times 10^{-42} L_{H\alpha}(\text{erg s}^{-1}) \quad (1)$$

(Kennicutt 1998) then gives $\text{SFR} = 0.09 M_{\odot} \text{ yr}^{-1}$. This assumes that the $H\alpha$ emission is completely driven by UV radiation from young stars, which may not be the case (e.g., Ferland et al. 2009), and that there is no intrinsic absorption. A violation of the former assumption would give an overestimate of the SFR, while a violation of the latter would give an underestimate. We compared the derived SFR to the mass cooling rate estimated from the X-ray observations by fitting the spectrum of the cool filament with a VAPEC plus a cooling flow VMCFLOW model, with the abundances fixed at the best fitting values for the total diffuse emission given in § 4.2.4. This gives a mass cooling rate in the gas of $0.41 \pm 0.07 M_{\odot} \text{ yr}^{-1}$. One concern with this result is that fitting a multi-temperature gas with a single cooling flow component may boost the inferred mass accretion rate. Unfortunately, we were unable to obtain a fit with reasonable parameter constraints from the *Chandra* data using a model combining an APEC and two VMCFLOW components. We therefore consider the mass accretion rate inferred from the fit to *XMM-Newton* RGS data described in § 4.2.4. From the two cooling flow components, we infer upper limits on the mass accretion rate of $< 0.45 M_{\odot} \text{ yr}^{-1}$ and $< 0.25 M_{\odot} \text{ yr}^{-1}$ for gas cooling above and below 0.4 keV, respectively (these are 2σ upper limits). Therefore, we conclude that the upper limit on the mass accretion rate from X-ray observations ($< 0.25 M_{\odot} \text{ yr}^{-1}$) and the star formation rate implied by $H\alpha$ observations ($\text{SFR} = 0.09 M_{\odot} \text{ yr}^{-1}$) are consistent with star formation being fueled by gas cooling down from X-ray temperatures.

For the cool gas to be buoyantly lifted by the X-ray cavities, its total mass must be less than the mass of gas displaced by the cavities. In particular, simulations indicate that the mass of gas buoyantly lifted by an AGN-blown bubble is about half the mass displaced by the bubble (Pope et al. 2010). We estimated the gas mass in the southern filament by fitting the spectra in this region with an APEC model and assuming that the cool gas is contained in a cylinder of radius 3.5 kpc and length 9.2 kpc, with the axis in the plane of the sky. The emission is dominated by the cool gas in this region, and accounting for the projected hot gas did not significantly change our results. We find a total gas mass of $M_{fil} = 1.5 \times 10^8 M_{\odot}$. A similar fit to an annulus surrounding the southwestern intermediate cavity gives an average electron density of $n_e = 0.022 \text{ cm}^{-3}$, giving a total mass of displaced gas $M_{disp} = 1.6 \times 10^8 M_{\odot}$, similar to the mass of gas in the filament. Thus, M_{fil} is larger than the value predicted by simulations ($\sim 0.5 M_{disp}$)

by a factor of two. We note that deep observations of the buoyantly lifted filaments in M87 reveal that they have a fine filamentary structure (Forman et al. 2007), in contrast with the solid cylindrical geometry we have assumed above (Werner et al. 2010 argue that the filling factor in M87 is of order unity in most regions, although they find a filling factor less than unity in some regions where there is fine filamentary structure). If the filling factor is less than unity then M_{fil} will be smaller by the same fraction. We conclude that the gas mass of the cool filament to the south is consistent with having been buoyantly lifted by the intermediate southwestern cavity, and is consistent with simulations if the filling factor is on the order of ~ 0.5 . We also note that if the filament has indeed been buoyantly lifted by the intermediate cavity then the filament, and hence the trajectory of the intermediate cavity, cannot lie far from the plane of the sky without assuming a small filling factor, since the length of the filament (and hence the volume it occupies) grows with inclination angle.

5.5. The Offset of the Central AGN

As noted in § 3, the central AGN is offset ~ 0.5 kpc southeast of the line defined by the X-ray cavities (see Figure 2). It is also offset from the center points of the elliptical edges defined by both the 1.5 kpc and 10 kpc shock fronts (which are each roughly coincident with the line defined by their respective cavity pairs), by about $2.3''$ (400 pc) for the 1.5 kpc shock and $7.5''$ (1.15 kpc) for the 10 kpc shock. A comparison of the *Chandra* image with the optical *Sloan Digital Sky Survey* image (Adelman-McCarthy et al. 2008) shows that the centroid of the optical emission is coincident with the AGN, and is separated from the center points of the elliptical X-ray shock fronts. This suggests that the cD galaxy has some peculiar velocity relative to the ICM, and that the AGN has moved since first inflating the X-ray cavities. The initial outburst that inflated the inner cavities occurred about 3×10^6 yr ago (see Table 2). Since then, the AGN has traveled about 400 pc in projection. This requires a relative velocity between the galaxy and the ICM of at least $\sim 130 \text{ km s}^{-1}$ (this is a lower limit since we measure the projected velocity). Similarly, the 10 kpc shock implies a relative velocity of $\sim 100 \text{ km s}^{-1}$. This is smaller than the host group's (NGC 5846) velocity dispersion (322 km s^{-1} , Mahdavi et al. 2005), and the relative radial velocity between NGC 5813 and NGC 5846 ($\sim 260 \text{ km s}^{-1}$), and is therefore a reasonable peculiar velocity for the cD galaxy relative to the group mean (or for the flow velocity of the ICM gas). We suggest that during the last $\sim 2 \times 10^7$ yr there has been a relative motion between the NGC 5813 galaxy and its ICM, from northwest to southeast, in projection, with the central AGN driving outbursts (i.e., inflating cavities into the ICM) at two locations (the outer cavities and edge are too poorly resolved to accurately measure the location of the associated outburst). The relative velocity may be due to the peculiar velocity of the cD relative to the group mean, or to bulk gas motions or gas sloshing of the ICM, or both. We note that once the outburst begins and the cavities are initially inflated, the location at which the energy is injected into the cavities is unimportant. The AGN may continue to move off of the axis

of symmetry of a pair of cavities while still depositing energy into them, driving their expansion and the resulting shocks.

5.6. Outburst Energy

During an AGN outburst, the jets inflate cavities in the ICM, which do work on the surrounding gas and drive shocks. It is convenient to regard the work done by the expanding lobes as “shock energy”, in which case the outburst energy that is available to heat the ICM is deposited to the ICM in two forms: the internal energy of the X-ray cavities and the shock energy. Since NGC 5813 shows both cavities and shocks from two distinct outbursts, we can compare the total energy, mean power, and the energy budget between shocks and cavities for each outburst. The shock energy can be roughly estimated from the pressure increase across the shock front. If a total energy E is added to a gas of volume V the pressure increase is roughly $\Delta P \sim E/V$. For a shock with a known Mach number, the ratio of the post- and pre-shock pressure $f_P = (P + \Delta P)/P$ is given by the Rankine-Hugoniot shock jump conditions. The total shock energy is therefore

$$E \approx PV(f_P - 1). \quad (2)$$

As a consistency check, we compare the estimated shock age, total energy, and mean power with results from our hydrodynamical model in Table 2. The shock age $t_{\text{age,est}}$ is estimated as the travel time from the current position of the shock front to the center point of the elliptical shock edge, assuming a constant Mach number and a sound speed of $c_s = 416 \text{ km s}^{-1}$ for a $kT = 0.65 \text{ keV}$ gas. The shock energy $E_{\text{sh,est}}$ is estimated using equation 2, assuming a prolate ellipsoidal geometry for the volume contained within the shock front with semi-major and -minor axes of $1.44'$ (13.5 kpc) and $1.13'$ (10.5 kpc) for the 10 kpc shocks and $17.6''$ (2.7 kpc) and $11.7''$ (1.8 kpc) for the 1.5 kpc shocks. Pressures were taken from the azimuthal pressure profile shown in Figure 10. Although the energies we give from the hydrodynamical model represent the total outburst energy, the point explosion model minimizes the internal energy in cavities, such that the energy in the central cavity is only a few percent of the total outburst energy. The model energy is therefore a very good approximation of the shock energy, and we refer to it as such. The model shock energies $E_{\text{sh,model}}$ were scaled to account for the difference in total volume for the spherically symmetric model as compared to the observed elliptical edges, and for the lower average pressure along the elliptical shock fronts, which cover a range in radii, assuming the shock energy scales as in equation 2 (these effects somewhat balance each other, as the volume correction increases the total energy, while the pressure correction decreases it). The correction factors are between 15–40%. The estimated and model shock energies and mean powers agree reasonably well, within factors of a few, demonstrating the consistency between rough estimates and results from our point explosion hydrodynamical model.

Table 2 indicates that the shock energy for the current outburst is more than an order of magnitude smaller than for the previous outburst. The mean power of the current outburst is also less than that of the previous

outburst, by about a factor of six ($1.5 \times 10^{42} \text{ erg s}^{-1}$ versus $1.0 \times 10^{43} \text{ erg s}^{-1}$, where we take the mean outburst power to be the sum of the shock energy and the $3PV$ internal energy of the cavities divided by the shock model ages). The lower shock energy of the most recent outburst may indicate that it is ongoing, having only deposited $\sim 1/40$ of its expected total energy output into the observed shocks (assuming that the current outburst is similar to the previous one). However, the lower shock energy may simply be a result of the lower mean power of the current outburst. We note that from X-ray observations of elliptical galaxies Allen et al. (2006) find evidence that accretion flows around central AGN are stable over a few million years, whereas we find that the mean jet power varies on time scales of $\sim 10^7 \text{ yr}$ (the time between outbursts).

We wish to compare the energy in shocks to the energy in the X-ray cavities for each outburst. The total internal energy of the cavities is roughly 3 times the mechanical energy (PV) required to inflate the cavities (McNamara & Nulsen 2007), which is given in Table 3. We find total cavity internal energies of $8.6 \times 10^{56} \text{ erg}$ and $7.8 \times 10^{55} \text{ erg}$ for the outbursts that produced the intermediate and inner cavities, respectively. Thus, the total internal energy in cavities is roughly 30% of the shock energy for the previous outburst and 1.3 times the shock energy for the current outburst. This is consistent with the current outburst being young, with the jets actively inflating the inner cavities and driving the 1.5 kpc shock, whereas for the previous outburst the shock has detached from the cavities, which rise buoyantly and lose energy as they age. We note that while our point explosion shock model is only approximate, so that the shock energies are somewhat uncertain, the relative sense of the energies is correct. Therefore, the larger fraction of total energy in cavities in the current outburst (as compared to the previous one) is a robust result.

For the outermost pair of cavities, the total internal energy in the cavities is $\sim 9.6 \times 10^{56} \text{ erg}$, on the order of the total energy of the intermediate cavities. However, 80% of this energy is contained in the northeastern cavity. While it is in principle possible for the mechanical energy to differ between paired cavities from the same outburst, the measurements for the southwestern cavity are uncertain since it is only marginally detected. Furthermore, such a large difference is not seen in the inner and intermediate cavity pairs. As discussed in § 5.3, the outer cavities may be in the process of breaking apart, and the outer northeastern cavity may have been re-energized by the intermediate cavity, making the measured mechanical energy (and hence the internal energy) uncertain.

We conclude that the lower total energy of the most recent outburst, as compared to the previous outburst, suggests that the outburst is ongoing, though this may simply be an effect of the lower mean power. Although the luminosity of the central source is low (see § 4.2.5), it may be in a short term quiescent state or heavily obscured, and does not rule out an ongoing outburst. AGN luminosities are known to vary by several orders of magnitude over very short time scales (e.g., Harris et al. 2009). Results from our 1D hydrodynamical simulations suggest that the mean power over longer timescales ($\sim 10^7 \text{ yr}$) can also vary significantly between outbursts,

even in an otherwise relaxed system like NGC 5813.

5.7. The Balance Between Heating and Cooling in the ICM

As noted in § 5.6, the total mechanical energy output of the AGN that is available to heat the ICM is primarily in two forms: the internal energy of X-ray cavities, which rise buoyantly after being inflated by jets from the AGN, and the “shock energy”, from shocks driven by the rapid inflation of the cavities. When and where the internal energy of the X-ray cavities gets transferred to the ICM is not well understood. In contrast, the local heat input at the shock front can be calculated directly from the Mach number. Furthermore, shock heating has two desirable features. First, the gas is more strongly heated in the core where Mach numbers are larger, close to the central AGN, which is the region of interest for regulating feedback between the ICM and the central SMBH. Second, the heating is roughly isotropic (as opposed to heating with jets or with the internal energy of the X-ray cavities). We therefore consider the energy input due to shocks, which, as we show in § 5.6, contain 40–80% of the total outburst energy in NGC 5813 (for a detailed discussion of heating with AGN outburst shocks see David et al. 2001).

To balance radiative cooling with AGN feedback shocks, the average outburst power must be on the order of or larger than the rate of radiative cooling. We estimated the radiative cooling rate as the X-ray luminosity, which we obtained by fitting the spectrum from the total emission within $170''$ (26.3 kpc) with an absorbed APEC model (using a VAPEC or two APEC model did not significantly change the resulting luminosity). The derived X-ray luminosity of $L_X = 5.4 \times 10^{41} \text{ erg s}^{-1}$ within 26 kpc implies a mean cooling time of $t_{\text{cool}} = 1.0 \text{ Gyr}$ (where we take the cooling time to be the time it would take to radiate away all of the internal energy of the gas at the current luminosity). For the 10 kpc shocks, we calculate the total shock energy to be $\sim 3 \times 10^{57} \text{ erg}$ (see § 5.6). Therefore, only 6 such outbursts are needed per cooling time to provide enough energy to completely offset radiative cooling with shocks alone within 26 kpc. The time between outbursts given by both the buoyant rise times of the cavities (Table 3) and, more reliably, from hydrodynamical simulations of the shocks (Table 2) is on the order of 10^7 yr , allowing 100 shocks per cooling time, more than is needed to provide the necessary energy.

While results from the 10 kpc shocks indicate that there is sufficient energy in shocks alone to offset radiative cooling, there are two points that must be considered. First, as discussed in § 5.6, the observed shocks suggest that the current and previous outburst shock energies differ in strength by more than an order of magnitude (although the most recent outburst may be ongoing). Furthermore, only some fraction of the total shock energy will go into heating the gas within the cooling radius, and for weak shocks this fraction is relatively small ($\lesssim 10\%$). We therefore consider the *local* balance of shock heating and radiative cooling for each shock. The primary effect of radiative cooling is to reduce the entropy of the gas. To offset cooling, the heating mechanism is required to increase the entropy by at least this amount. Shocks will also affect the kinetic, thermal, and potential

energy of the gas, but these effects are transient, and for heating it is the change in entropy of the gas that is relevant. Hence, the entropy increase ΔS caused by a weak shock can offset a radiative heat loss of $\Delta Q \simeq T \Delta S$, where T is the gas temperature. Expressed as a fraction of the gas thermal energy, the effective heat input from one shock is therefore $(T \Delta S)/E = \Delta \ln(P/\rho^\gamma)$, where E is the thermal energy and γ is the adiabatic index. For the 10 kpc shocks, the Mach numbers given in Table 2 imply a change in $\ln(P/\rho^\gamma)$ across the shock front of $\sim 5\%$. Therefore, to balance the total entropy decrease of the gas about $1/0.05 = 20$ outbursts are needed per *local* cooling time to completely offset cooling with shock heating. By the same argument, 10 outbursts per cooling time are needed to replace the thermal energy of the gas at the 1.5 kpc shock. The cooling time of the pre-shock gas just outside the 10 kpc shock edge is $9 \times 10^8 \text{ yr}$, so an outburst interval of 10^7 yr gives 90 shocks per local cooling time. For the 1.5 kpc shock, the pre-shock gas cooling time is $2 \times 10^8 \text{ yr}$, giving 20 shocks per cooling time. Thus, we conclude that shock heating alone is sufficient to offset radiative cooling of the gas within the 1.5 kpc and 10 kpc shock fronts, consistent with previous suggestions that shocks can offset cooling close to central AGN (Nulsen et al. 2007). The X-ray cavities rise buoyantly, and release their internal energy to heat the ICM gas at larger radii. Although previous studies have found other systems where there is enough total shock energy to offset radiative cooling (e.g., M87 Forman et al. 2005, with M87 also showing concentric shock fronts from multiple AGN outbursts; Hydra A Nulsen et al. 2005), here we explicitly show that the fraction of shock energy that goes into heating the gas (5–10%) is sufficient to balance radiative cooling locally at the shock fronts. The outburst interval is short enough for such shocks to offset cooling over much longer timescales. This demonstrates that AGN feedback can operate to heat the gas within galaxies, as well as the more extended ICM in clusters, as required by some galaxy formation models (e.g., Kormendy et al. 2009).

6. SUMMARY

We have presented results based on *Chandra*, *VLA*, *GMRT*, and *SOAR* observations of NGC 5813, the dominant member of a galaxy group. The ICM shows clear signatures from three distinct AGN outbursts in an otherwise relaxed system (including two shocks with detectable temperature jumps), making this object uniquely well-suited to the study of AGN feedback. We find the following:

1. Three pairs of collinear cavities, where each pair is associated with a distinct AGN outburst. The inner two pairs are associated with unambiguous shocks (with Mach numbers $M_i = 1.7$, $M_o = 1.5$), with clear temperature rises, that can be directly detected from the X-ray data. The outermost cavity pair also has an associated surface brightness edge. The properties of this edge are consistent with an old shock associated with the outermost cavities, although the current data do not rule out other interpretations (e.g., a transition region from the galactic atmosphere to the extended group atmosphere). The locations of the cavities and the

- shocks indicate an outburst interval of $\sim 10^7$ yrs.
2. Diffuse radio emission, filling the inner cavities at 1.36 GHz and 235 MHz and the intermediate cavities at 235 MHz. Radio emission from the outer cavities is not detected. This reflects the greater age of the relativistic particles in more distant cavities.
 3. A cool trail of gas that has been buoyantly lifted by the intermediate cavities. The gas is co-spatial with filaments seen in $H\alpha$ observations.
 4. The mean power of the current outburst is six times less than that of the previous outburst, indicating that the average jet power can vary significantly between outbursts, even in near “steady state” AGN feedback with regular outbursts in an otherwise dynamically relaxed system.
 5. The total heat energy input from shocks alone is sufficient to balance radiative cooling locally. This heating takes place in the core, close to the central AGN, which is the region of interest for regulating

feedback between the ICM and the central SMBH. Thus, for the first time, we explicitly show a system where shock heating alone can locally balance radiative cooling and regulate AGN feedback.

The financial support for this work was partially provided for by the Chandra X-ray Center through NASA contract NAS8-03060, and the Smithsonian Institution. We thank the staff of the *GMRT* for their help during the observations. *GMRT* is run by the National Centre for Radio Astrophysics of the Tata Institute of Fundamental Research. The *SOAR* Telescope is a joint project of Conselho Nacional de Pesquisas Científicas e Tecnológicas CNPq-Brazil, The University of North Carolina Chapel Hill, Michigan State University, and the National Optical Astronomy Observatory. AS and NW are supported by the National Aeronautics and Space Administration through Chandra/Einstein Postdoctoral Fellowship Award Numbers PF9-00070 and PF8-90056 issued by the *Chandra* X-ray Observatory Center, which is operated by the Smithsonian Astrophysical Observatory for and on behalf of the National Aeronautics and Space Administration under contract NAS8-03060.

REFERENCES

- Adelman-McCarthy, J. et al. 2008, *ApJS*, 175, 297
- Allen, S. W., Dunn, R. J. H., Fabian, A. C., Taylor, G. B., & Reynolds, C. S. 2006, *MNRAS*, 372, 21
- Anders, E., & Grevesse, N. 1989, *Geochimica et Cosmochimica Acta*, 53, 197
- Balmaverde, B. & Capetti, A. 2006, *A&A*, 447, 97
- Birzan, L., McNamara, B. R., Nulsen, P. E. J., Carilli, C. L., & Wise, M. W. 2008, *ApJ*, 686, 859
- Birzan, L., McNamara, B. R., Nulsen, P. E. J., & Wise, M. W. 2009, pre-print (arXiv:0909.0397)
- Blanton, E. L., Randall, S. W., Douglass, E. M., Sarazin, C. L., Clarke, T. E., & McNamara, B. R. 2009, *ApJL*, 697, 95
- Blanton, E. L., Sarazin, C. L., McNamara, B. R. 2003, *ApJ*, 585, 227
- Böhringer, H. et al. 2004, *A&A*, 425, 367
- Brunetti, G., Setti, G., & Comastri, A. 1997, *A&A*, 325, 898
- Buote, D. 1999, *MNRAS*, 309, 685
- Cavagnolo, K. W., McNamara, B. R., Nulsen, P. E. J., Carilli, C. L., Jones, C., & Birzan, L. 2010, (in prep.)
- Churazov, E., Brüggén, M., Kaiser, C. R., Böhringer, H., & Forman, W. 2001, 554, 261
- Churazov, E., Forman, W., Vikhlinin, A., Tremaine, S., Gerhard, O., & Jones, C. 2008, *MNRAS*, 388, 1062
- Churazov, E., Sunyaev, R., Forman, W., & Böhringer, H. 2002, *MNRAS*, 332, 729
- Churazov, E., Tremaine, S., Forman, W., Gerhard, O., Das, P., Vikhlinin, A., Jones, C., Böhringer, H., & Gebhardt, K. 2010, *MNRAS*, 404, 1165
- David, L. P., Nulsen, P. E. J., McNamara, B. R., Forman, W., Jones, C., Ponman, T., Robertson, B., & Wise, M. 2001, *ApJ*, 557, 546
- Donahue, M., Sun, M., O’Dea, C. P., Voit, G. M., & Cavagnolo, K. W. 2007, *AJ*, 134, 14
- Dunn, R. J. H., Allen, S. W., Taylor, G. B., Shurkin, K. F., Gentile, G., Fabian, A. C., & Reynolds, C. S. 2010, *MNRAS*, 404, 180
- Emsellem, E. et al. 2007, *MNRAS*, 379, 401
- Fabian, A. C., Hu, E. M., Cowie, L. L., & Grindlay, J. 1981, *ApJ*, 248, 47
- Fabian, A. C., Sanders, J. S., Crawford, C. S., Conselice, C. J., Gallagher, J. S., & Wyse, R. F. G. 2003, *MNRAS*, 344, 48
- Fabian, A. C., Sanders, J. S., Taylor, G. B., Allen, S. W., Crawford, C. S., Johnstone, R. M., & Iwasawa, K. 2006, *MNRAS*, 366, 417
- Ferland, G. J., Fabian, A. C., Hatch, N. A., Johnstone, R. M., Porter, R. L., van Hoof, P. A. M., & Williams, R. J. R. 2009, *MNRAS*, 392, 1475
- Finoguenov, A., David, L. & Ponman, T. 2000, *ApJ*, 188, 203
- Finoguenov, A., Reiprich, T. & Böhringer, H. 2001, *A&A*, 368, 749
- Finoguenov, A., Ruszkowski, M., Jones, C., Brüggén, M., Vikhlinin, A., Mandel, E. 2008, *ApJ*, 686, 911
- Forman, W., et al. 2007, *ApJ*, 665, 1057
- Forman, W., Nulsen, P., Heinz, S., Owen, F., Eilek, J., Vikhlinin, A., Markevitch, M., Kraft, R., Churazov, E., & Jones, C. 2005, *ApJ*, 635, 894
- Gastaldello, F., Buote, D. A., Humphrey, P. J., Zappacosta, L., Bullock, J. S., Brighenti, F., & Mathews, W. G. 2007, *ApJ*, 669, 158
- Giacintucci, S., Vrtilek, J. M., O’Sullivan, E., Raychaudhury, S., David, L. P., Venturi, T., Athreya, R., & Gitti, M. 2009, Proceedings of the conference “The Monster’s Fiery Breath: Feedback in Galaxies, Groups, and Clusters”, June 2009, Madison, Wisconsin, pre-print (arXiv:0909.0291)
- Giacintucci, S., et al. 2010, *ApJ* (in prep.)
- Gitti, M., O’Sullivan, E., Giacintucci, S., David, L. P., Vrtilek, J., Raychaudhury, S., Nulsen, P. E. J. 2010, *ApJ*, 714, 758
- Graham, J., Fabian, A. C., & Sanders, J. S. 2008, *MNRAS*, 386, 278
- Grevesse, N., & Sauval, A. J. 1998, *Space Sci. Rev.*, 85, 161
- Harris, D. E., Cheung, C. C., Stawarz, Lukasz, Biretta, J. A., & Perlman, E. S. 2009, *ApJ*, 699, 305
- Humphrey, P. J., Buote, D. A., & Canizares, C. R. 2004, *ApJ*, 617, 1047
- Kalberla, P. M. W., Burton, W. B., Hartmann, D., Arnal, E. M., Bajaja, E., Morras, R., Pöppel, W. G. L. 2005, *A&A*, 440, 775
- Kennicutt, R. C. 1998, *ARA&A*, 36, 189
- Kirkpatrick, C. C., Gitti, M., Cavagnolo, K. W., McNamara, B. R., David, L. P., Nulsen, P. E. J., & Wise, M. W. 2009, *ApJL*, 707, 69
- Kormendy, J., Fisher, D. B., Cornell, M. E., & Bender, R. 2009, *ApJS*, 182, 216
- Lauer, T. R. et al. 2007, *ApJ*, 664, 226
- Magliocchetti, M. & Brüggén, M. 2007, 379, 260
- Mahdavi, A., Trentham, N., & Tully, R. B. 2005, 130, 1502
- Mazzotta, P., Rasia, E., Moscardini, L., & Tormen, G. 2004, *MNRAS*, 354, 10
- McNamara, B. & Nulsen, P. J. E. 2007, *ARA&A*, 45, 117
- Nulsen, P. E. J., Hambrick, D. C., McNamara, B. R., Rafferty, D., Birzan, L., Wise, M. W., & David, L. P. 2005, *ApJ*, 625, 9
- Nulsen, P. J. E., Jones, C., Forman, W. R., David, L. P., McNamara, B. R., Rafferty, D. A., Birzan, L., & Wise, M. W. 2007, Heating versus Cooling in Galaxies and Clusters of Galaxies, ed. H. Böhringer, G. W. Pratt, A. Finoguenov, & P. Schuecker (Berlin: Springer), 210

- Peterson, J. R., & Fabian, A. C. 2006, PhR, 427, 1
- Peterson, J. R., Paerels, F. B. S., Kaastra, J. S., Arnaud, M., Reiprich, T. H., Fabian, A. C., Mushotzky, R. F., Jernigan, J. G., & Sakellou, I. 2001, A&A, 365L, 104
- Pope, E. C. D., Babul, A., Pavlovski, G., Bower, R. G., & Dotter, A. 2010, pre-print (arXiv:1004.2050v2)
- Ptak, A. 2001, AIPC, 599, 326
- Randall, S. W., Clarke, T. E., Nulsen, P. J. E., Owers, M. S., Sarazin, C. L., Forman, W. R., & Murray, S. S. 2010, ApJ, (submitted)
- Randall, S. W., Jones, C., Kraft, R., Forman, W. R., & O’Sullivan, E. 2009a, ApJ, 696, 1431
- Randall, S. W., Jones, C., Markevitch, M., Blanton, E. L., Nulsen, P. E. J., & Forman, W. R. 2009b, ApJ, 700, 1404
- Randall, S., Nulsen, P., Forman, W., Jones, C., Machacek, M., Murray, S., & Maughan, B. 2008, ApJ, 688, 208
- Rasia, E., Mazzotta, P., Bourdin, H., Borgani, S., Tornatore, L., Ettori, S., Dolag, K. & Moscardini, L. 2008, ApJ, 674, 728
- Sanders, J. S. & Fabian, A. C. 2007, MNRAS, 381, 1381
- Sanders, J. S., & Fabian, A. C., & Taylor, G. B. 2009, MNRAS, 396, 1449
- Simionescu, A., Werner, N., Böhringer, H., Kaastra, J. S., Finoguenov, A., Brüggén, M., & Nulsen, P. E. J. 2009, A&A, 493, 409
- Simionescu, A., Werner, N., Finoguenov, A., Böhringer, H., & Brüggén, M. 2008, A&A, 482, 97
- Sun, M., Donahue, M., & Voit, G. M. 2007, ApJ, 671, 190
- Sun, M., Voit, G. M., Donahue, M., Jones, C., Forman, W., & Vikhlinin, A. 2009, ApJ, 693, 1142
- Tonry, J. L., Dressler, A., Blakeslee, J. P., Ajhar, E. A., Fletcher, A. B., Luppino, G. A., Metzger, M. R., & Moore, C. B. 2001, ApJ, 546, 681
- Tran, H. D., Tsvetanov, Z., Ford, H. C., Davies, J., Jaffe, W., van den Bosch, F. C., & Rest, A. 2001, AJ, 121, 2928
- Vikhlinin, A., Markevitch, M., Murray, S. S., Jones, C., Forman, W., & Van Speybroeck, L. 2005, ApJ, 628, 655
- Vikhlinin, A., Markevitch, M., & Murray, S. S. 2001, ApJ, 551, 160
- Werner, N., et al. 2010, pre-print (arXiv:1003.5334)
- Werner, N., Zhuravleva, I., Churazov, E., Simionescu, A., Allen, S. W., Forman, W., Jones, C., & Kaastra, J. S. 2009, MNRAS, 398, 23

TABLE 1
SUMMARY OF THE RADIO OBSERVATIONS

| Radio telescope | Project | Observation date | Array | Frequency (MHz) | Bandwidth (MHz) | Integration time (min) | HPBW, PA ($'' \times ''$, $^\circ$) | rms ($\mu\text{Jy b}^{-1}$) |
|-----------------|---------|------------------|-------|-----------------|-----------------|------------------------|--|-------------------------------|
| GMRT | 14SGA01 | Aug 2008 | full | 235 | 8 | 100 | $16.5 \times 15.1, 74$ | 300 |
| VLA | AF0188 | Apr 1990 | A | 1490 | 50 | 45 | $1.3 \times 1.2, 28$ | 22 |
| VLA | AW0202 | Jan 1988 | B | 1360 | 50 | 30 | $4.9 \times 4.7, -84$ | 20 |
| VLA | AC0488 | Sept 1997 | C | 1360 | 50 | 6 | $27.4 \times 16.8, 53$ | 30 |
| VLA | AW0112 | Jun 1984 | C | 4860 | 50 | 8 | $5.0 \times 4.5, -4$ | 25 |

TABLE 2
PROPERTIES OF THE SHOCKS

| ID | r^a (kpc) | $\Delta\rho^b$ | M^c | $t_{\text{age,model}}^d$ (10^7 yr) | $E_{\text{sh,model}}^e$ (10^{57} erg) | W_{model}^f (10^{42} erg s $^{-1}$) | M_{acc}^g ($10^3 M_\odot$) | $t_{\text{age,est}}^h$ (10^7 yr) | $E_{\text{sh,est}}^i$ (10^{57} erg) | W_{est}^j (10^{42} erg s $^{-1}$) |
|------------|-------------|------------------------|-------|---------------------------------------|--|--|---------------------------------------|-------------------------------------|--|--|
| Inner, SE | 1.4 | $1.97^{+0.12}_{-0.12}$ | 1.71 | 0.3 | 0.06 | 0.6 | 0.3 | 0.2 | 0.2 | 2.7 |
| Middle, SE | 9.9 | $1.69^{+0.07}_{-0.07}$ | 1.48 | 1.4 | 2.2 | 5.0 | 8.2 | 1.6 | 3.0 | 5.9 |
| Middle, NW | 11.5 | $1.75^{+0.04}_{-0.03}$ | 1.53 | 1.3 | 3.3 | 8.0 | 22.4 | 1.6 | 3.0 | 5.9 |

^a Distance from the AGN to the shock front.

^b Density jump at shock front.

^c Mach number.

^d Shock age, from the hydrodynamical model. The point explosion approximation gives large Mach numbers at early times, so the shock ages are underestimated.

^e Shock energy, from the hydrodynamical model.

^f Mean shock power, from the hydrodynamical model.

^g Minimum accreted mass needed to power the model outburst (assuming 100% efficiency).

^h Shock age, estimated as the travel time from the current position to the center point of the elliptical shock edge. Since the current Mach number is used to give a constant velocity, the shock ages are overestimated.

ⁱ Shock energy, estimated using Equation 2.

^j Estimated mean shock power.

TABLE 3
PROPERTIES OF THE X-RAY CAVITIES

| ID | a^a (kpc) | b^b (kpc) | r^c (kpc) | t_{rise}^d (10^7 yr) | E_{mech}^e (10^{55} erg) |
|----------------------------|-------------|-------------|-------------|----------------------------------|--------------------------------------|
| Inner, SW | 0.95 | 0.95 | 1.3 | 0.6^f | 1.1 |
| Inner, NE | 1.03 | 0.93 | 1.4 | 0.7^f | 1.5 |
| Middle, SW | 3.9 | 3.9 | 7.7 | 3.6 | 15.3 |
| Middle-1 ^g , NE | 2.9 | 2.2 | 4.9 | 2.3 | 9.3 |
| Middle-2 ^g , NE | 2.8 | 2.4 | 9.3 | 4.4 | 4.1 |
| Outer ^h , SW | 5.2 | 3.0 | 22.2 | 10.4 | 6.0 |
| Outer, NE | 8.0 | 4.4 | 18.0 | 8.5 | 26.0 |

^a Semi-major axis.

^b Semi-minor axis.

^c Distance from central AGN.

^d Lower limit on the bubble rise time, assuming that each bubble rises at half the sound speed for a 0.65 keV gas.

^e PV mechanical energy required to inflate the cavity.

^f The cavity size is on the order of the distance to the AGN, and these cavities are likely still being or have only recently been inflated by the AGN, so the computed rise time is not a reliable estimate of the cavity age.

^g Part of a “split” or “Russian doll” cavity.

^h Cavity is only marginally detected, tabulated properties may not be reliable.

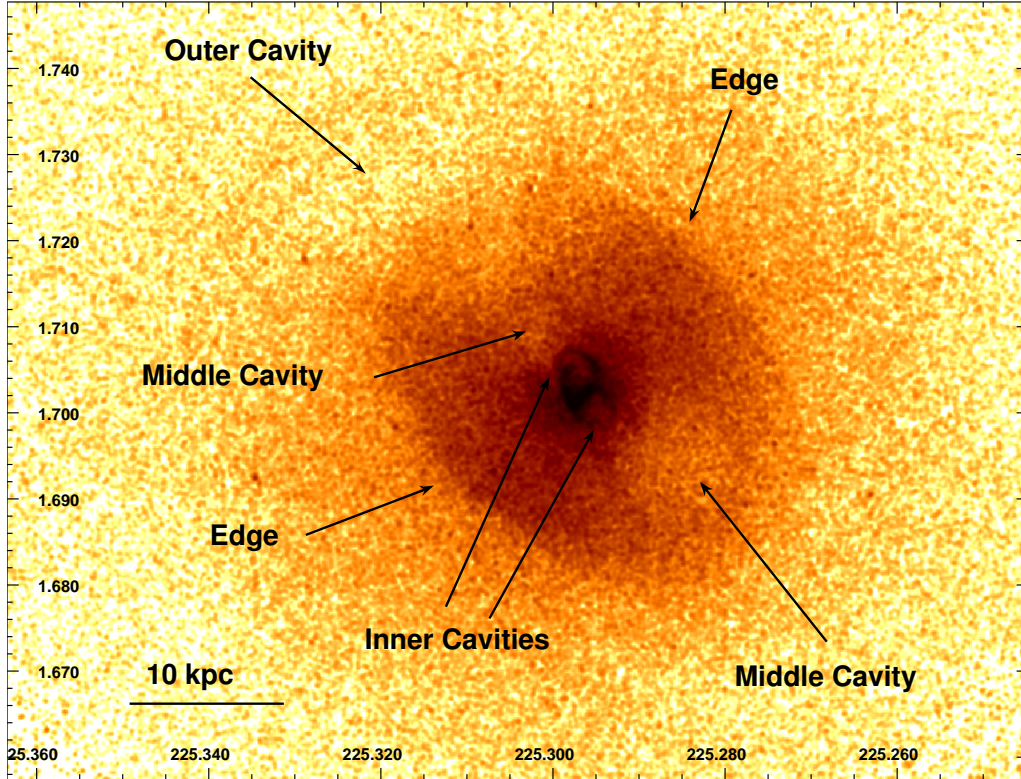


FIG. 1.— Exposure corrected, background subtracted 0.3–2 keV *Chandra* image of NGC 5813. The image has been smoothed with a $1.5''$ radius Gaussian and point sources have been filled-in by randomly drawing from a Poisson distribution fit to a local background annular region. The image shows two pairs of cavities, plus an outer cavity to the northeast, two sharp edges to the northwest and southeast, and bright rims around the pair of inner cavities.

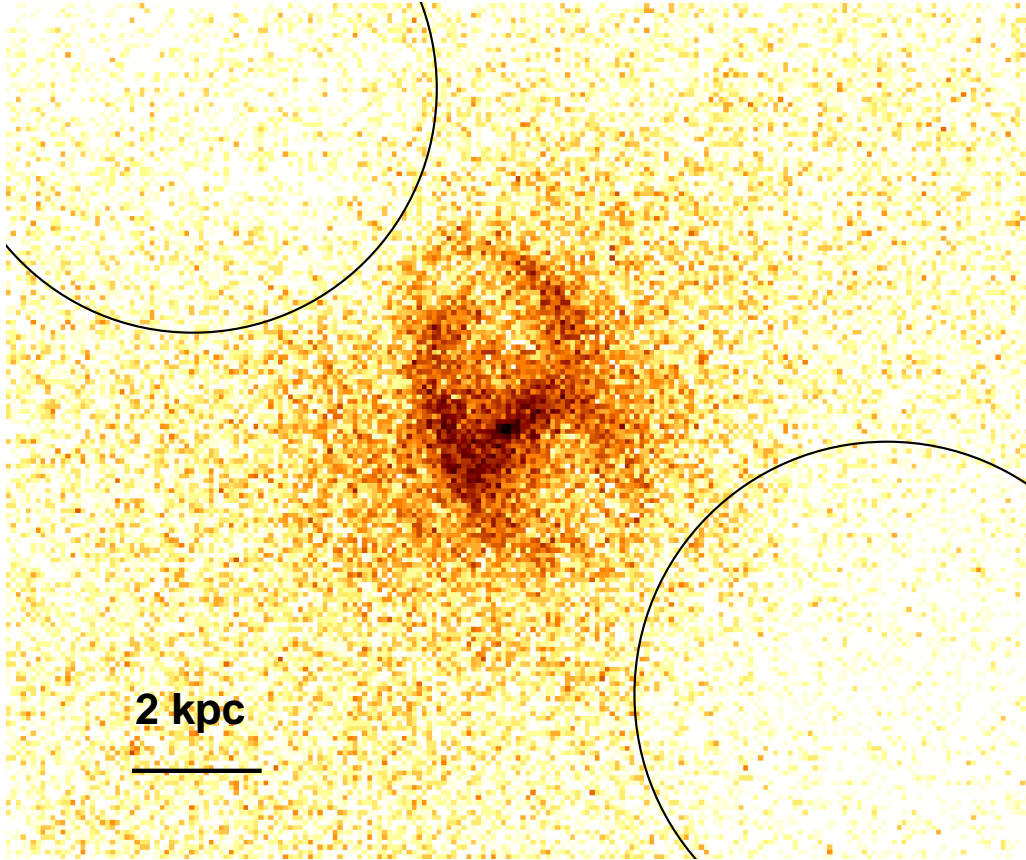


FIG. 2.— The core from the image in Figure 1, unsmoothed. The point-like AGN is visible, offset ~ 0.5 kpc southeast of the axis of symmetry of the inner cavities. There is a sharp edge just southeast of the AGN, and the two rings surrounding the inner cavities overlap to form an indented structure to the northwest. The black circles define the inner edges of the intermediate cavities.

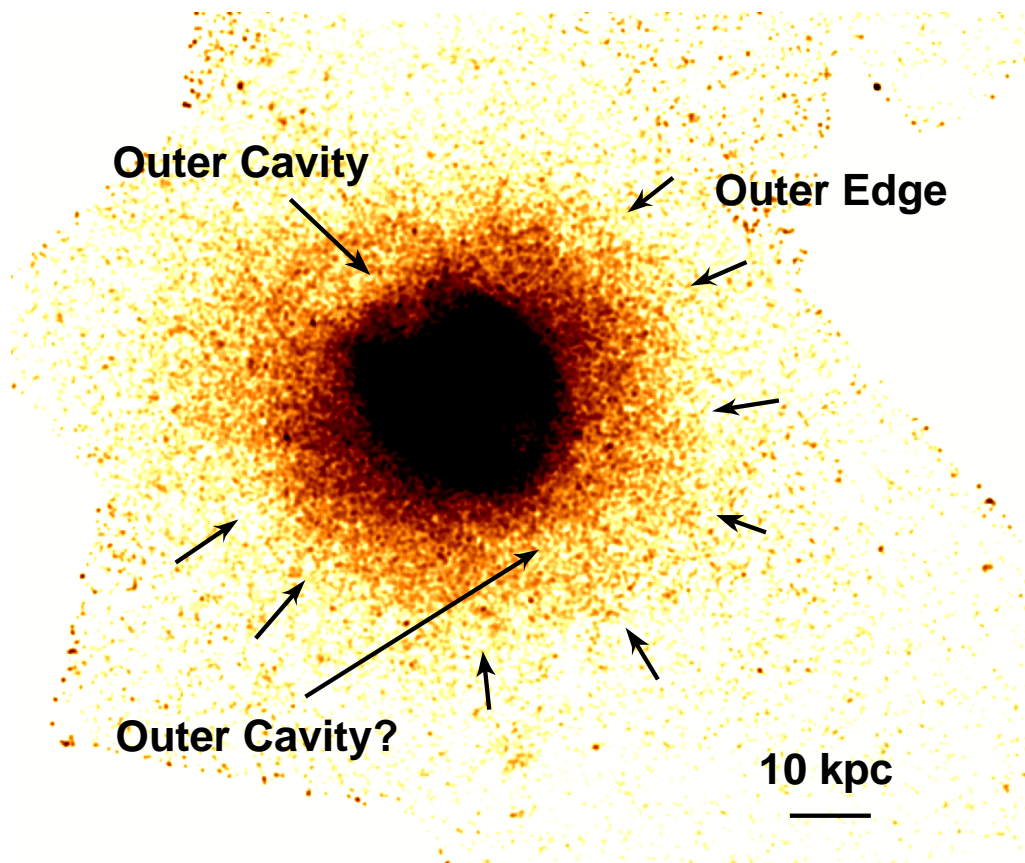


FIG. 3.— Same as Figure 1, but smoothed with a $3''$ radius Gaussian to show faint features in the outer regions. The image shows a weak outer cavity to the southwest, and a faint outer edge-like feature (indicated by the multiple short arrows) that encircles NGC 5813. To the northeast the edge structure is less clear, as there is brighter diffuse emission extending across the edge out to larger radii in this direction.

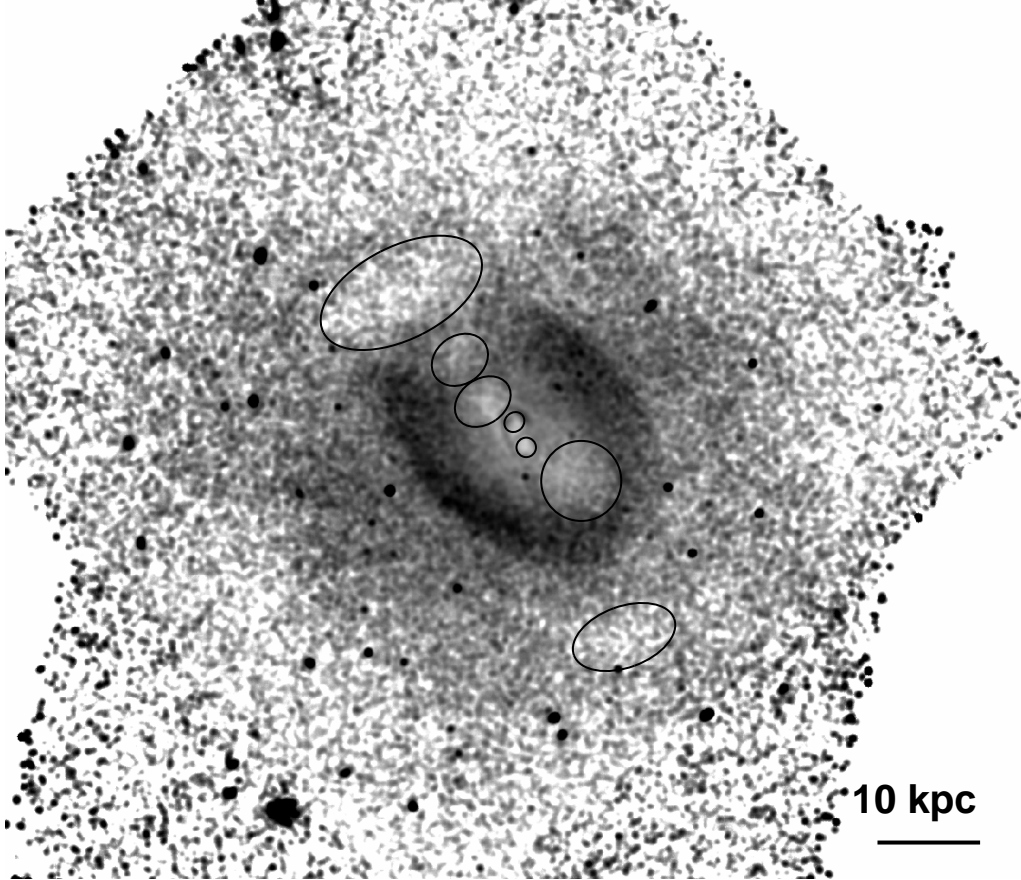


FIG. 4.— 0.3–2.0 keV *Chandra* image from Figure 1 (with sources included), divided by a fitted beta model and smoothed with a $6''$ Gaussian to more clearly show surface brightness fluctuations over a wider dynamic range. The cavity regions listed in Table 3 are overlaid for clarity. We see the two small inner cavities at ~ 1.5 kpc, the middle cavities (with the northeastern “Russian doll” cavity split into two pieces) at ~ 8 kpc, and the outermost cavities at ~ 20 kpc.

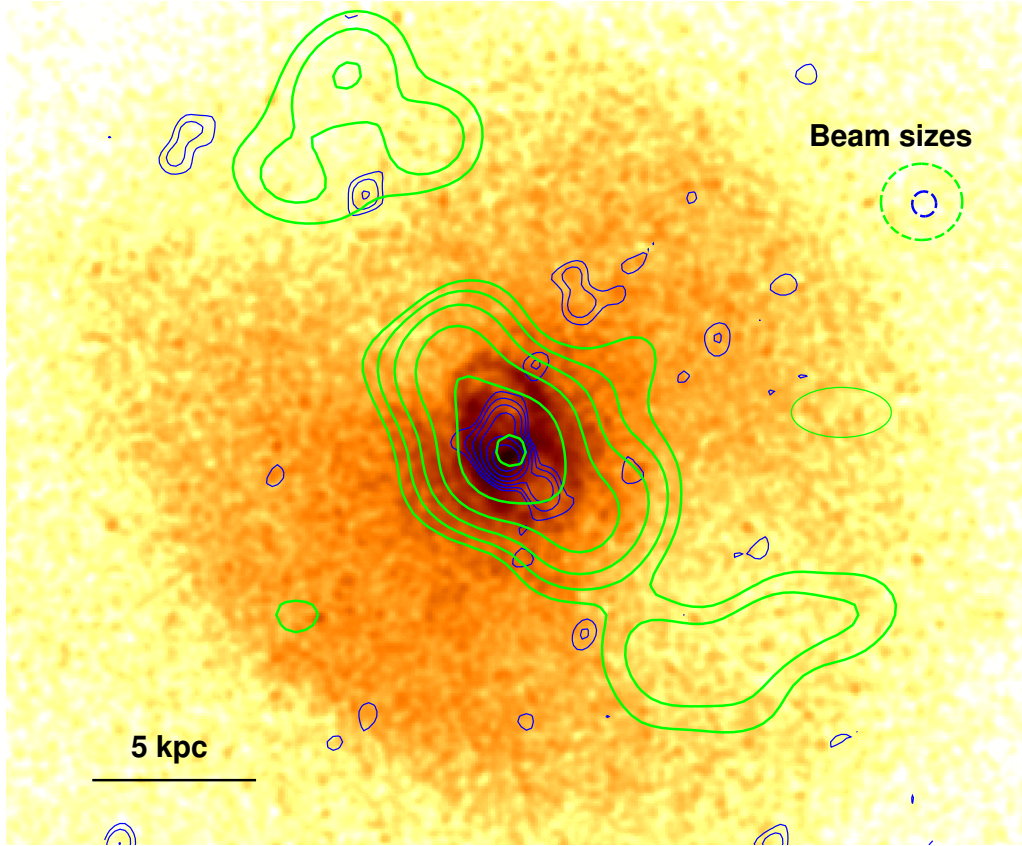


FIG. 5.— *Chandra* 0.3–2.0 keV image of the core, with 1.36 GHz *VLA* B array configuration (blue) and 235 MHz *GMRT* (green) contours overlaid. The contours start at 3σ and are spaced by a factor of two. Low frequency radio emission fills the intermediate cavities near the edge of the FOV, and emission at both frequencies fills the inner cavities. The central peak of the 1.36 GHz contours is coincident with the AGN, while the peak of the 235 MHz contours is northwest of the AGN, roughly coincident with the center point of the elliptical edge defined by the inner shock front. The dashed lines indicate the beam sizes for each radio observation.

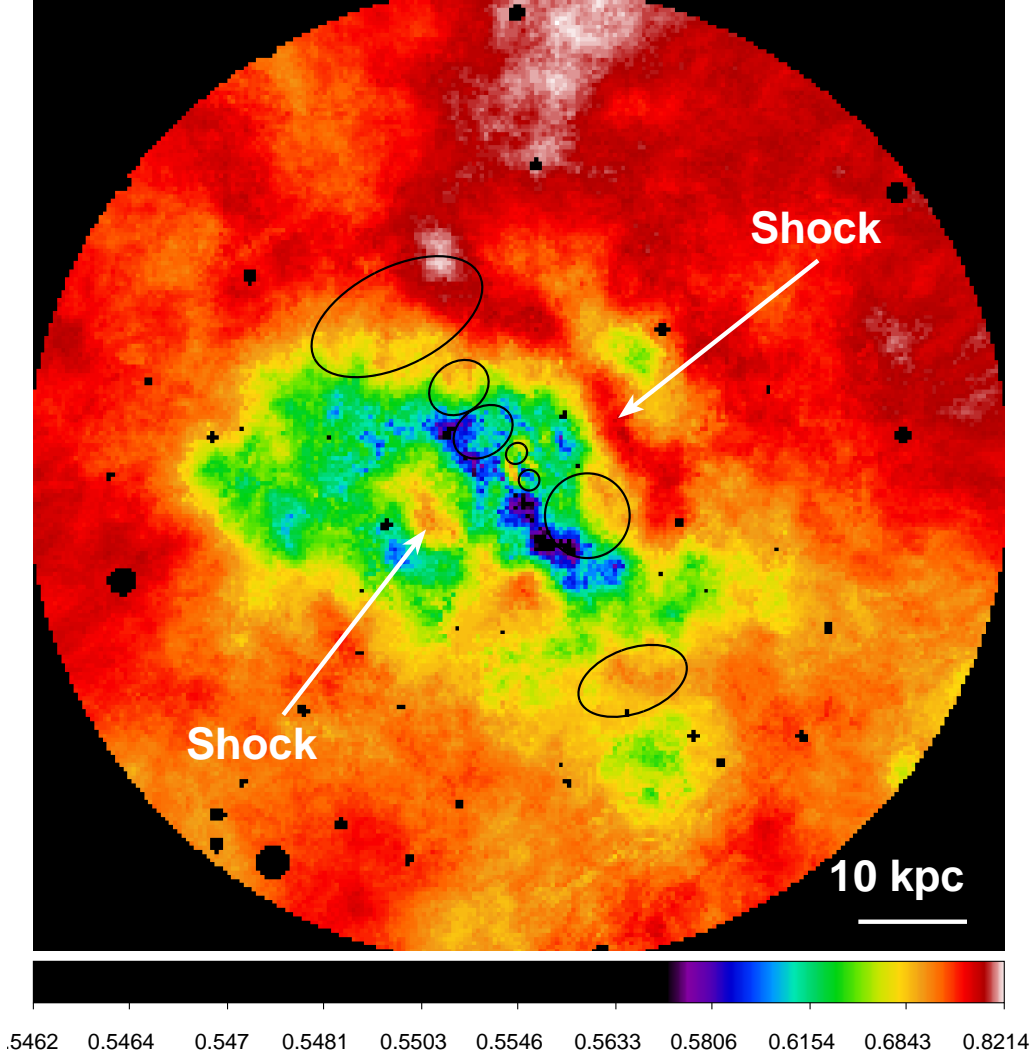


FIG. 6.— Temperature map derived from the ACIS-S3 data, with the cavity regions from Figure 4 overlaid. The color-bar gives the temperature in keV. The shocks stand out as temperature peaks coinciding with the surface brightness edges. Cooler gas follows the southeastern edges of the intermediate surface brightness cavities indicated in Figure 1.

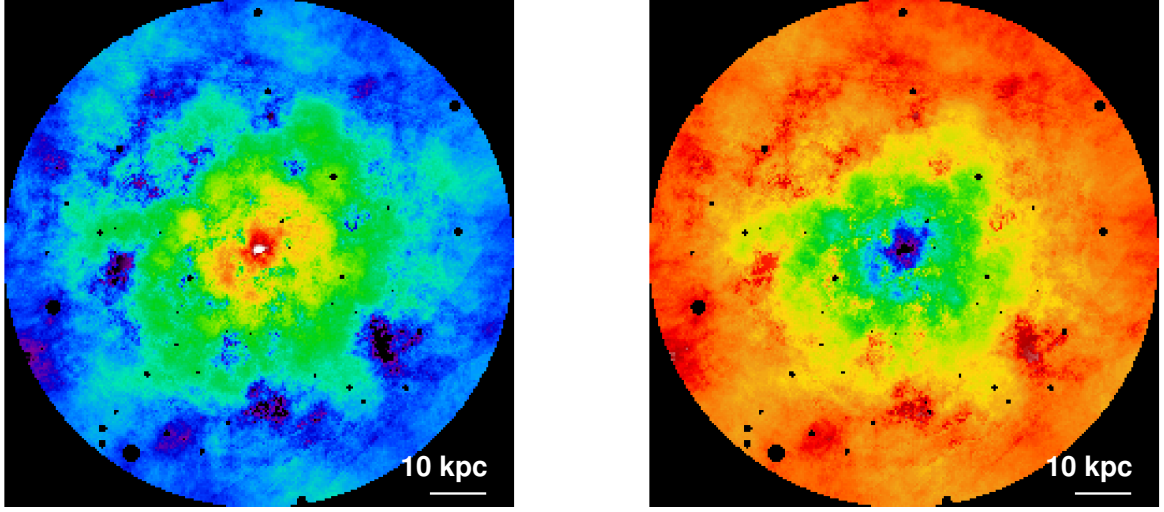


FIG. 7.— Pseudo pressure (left) and entropy (right) maps, in arbitrary units. The pressure map was calculated as $kTA^{1/2}$ and the entropy map as $kTA^{-1/3}$, where A is the APEC normalization scaled by the area of the extraction region. The pressure jumps at the 10 kpc shocks are visible ~ 10 kpc northwest and southeast of the central peak.

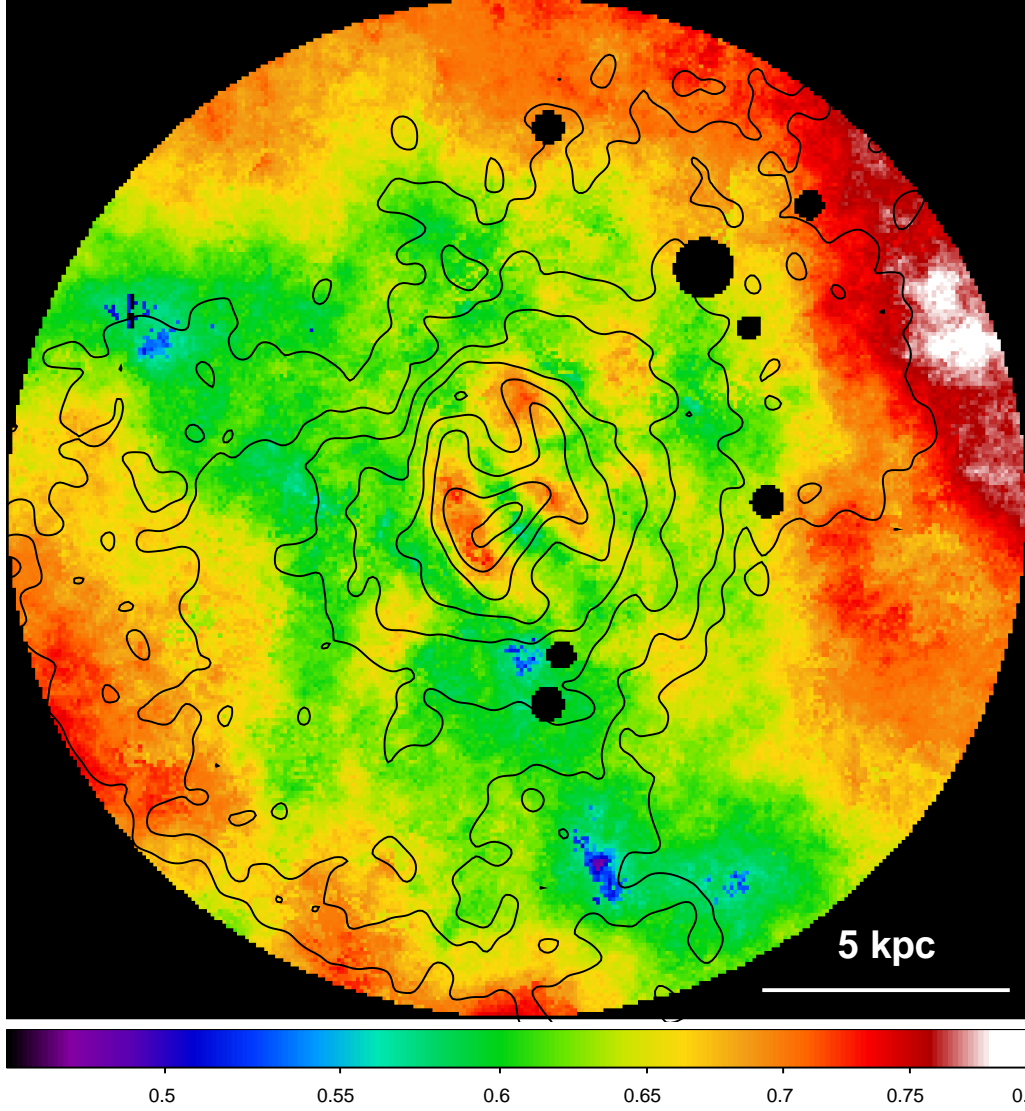


FIG. 8.— A high-spatial resolution temperature map of the core of NGC 5813, with *Chandra* X-ray 0.3–2.0 keV logarithmic surface brightness contours overlaid. The color-bar gives the temperature in keV. The bright rims surrounding the innermost cavities are revealed to contain hot gas, probably shock-heated by the central AGN during a recent outburst.

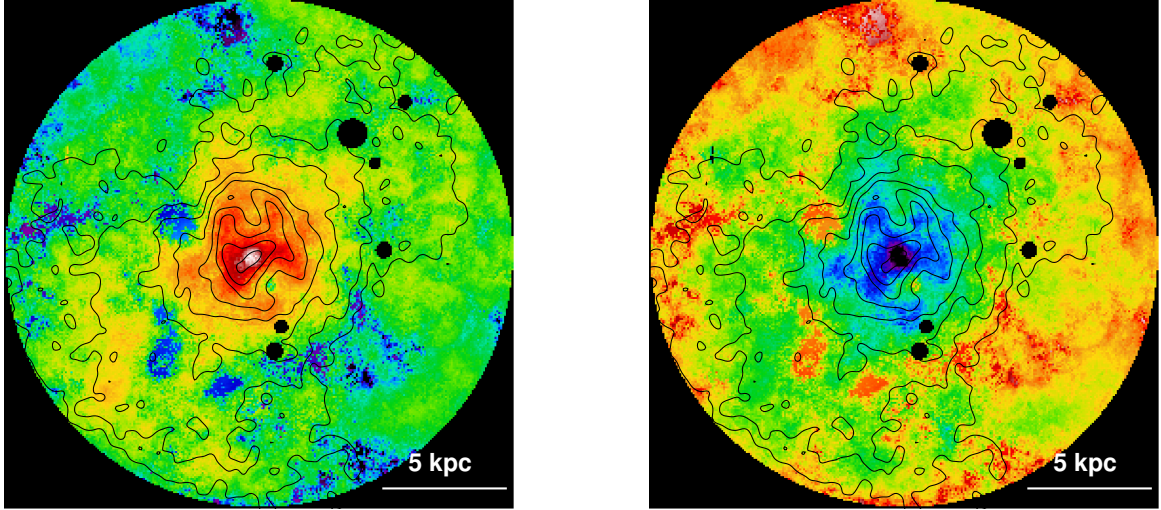


FIG. 9.— Pseudo pressure (left) and entropy (right) maps, in arbitrary units, derived as in Figure 7. X-ray surface brightness contours are overlaid in black. There is a sharp pressure jump coincident with the temperature jump southeast of the core seen in Figure 8, identifying this feature as a shock. Also visible are local pressure minima (and entropy maxima) at the location of the inner cavities, presumably due to the additional non-thermal pressure support from the radio emitting plasma in the cavities.

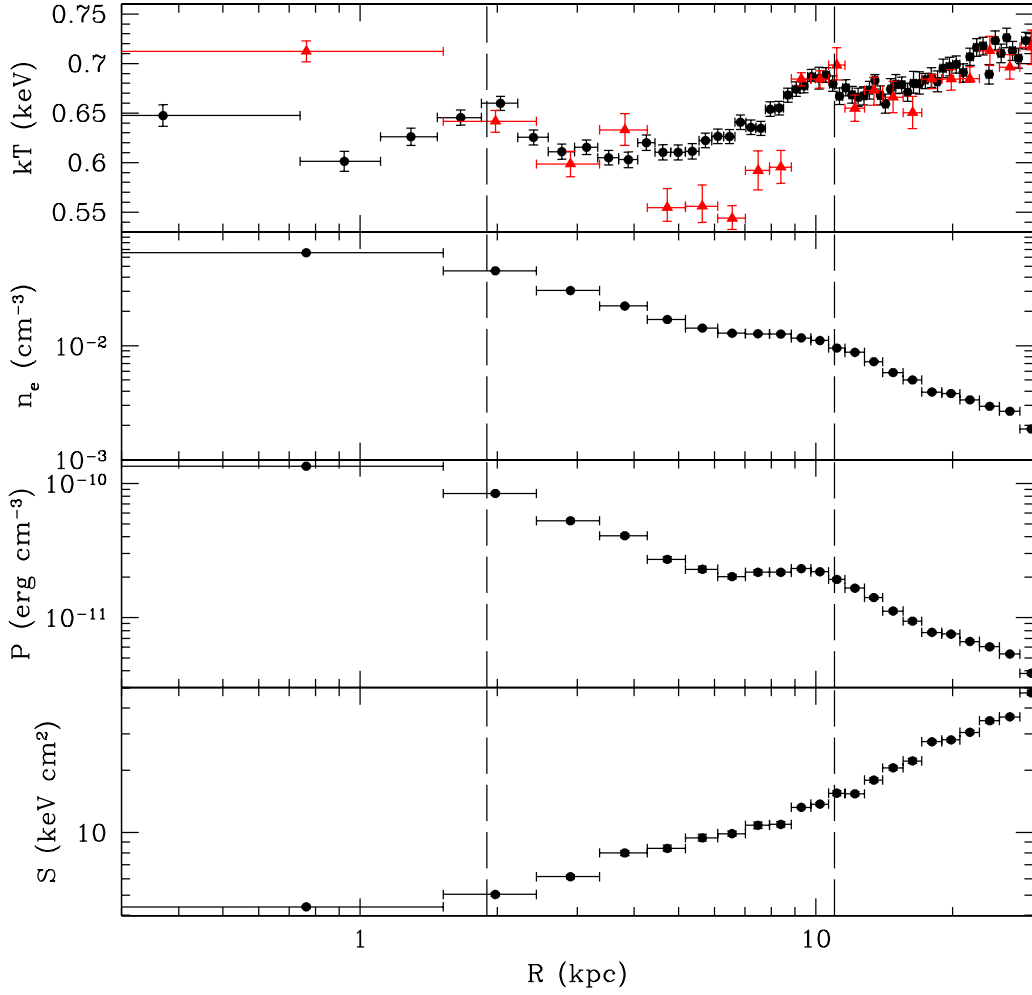


FIG. 10.— Azimuthally averaged radial profiles for (top to bottom) temperature, electron density, pressure, and entropy, extracted from circular annuli. The top panel shows the projected (black circles) and deprojected (red triangles) temperature profiles. All other panels show deprojected values. The vertical dashed lines mark the average radius of the 1.5 kpc (left) and 10 kpc (right) elliptical shock fronts indicated in Figure 1. The shocks are smeared over multiple bins due to their non-spherical structure. The temperature and pressure increase at each shock front. The temperature profiles show a central temperature spike, even though the region of the central AGN has been excluded from the fits. This is because the profile center is in the region of the hot overlapping rims of the central cavities, shown in Figure 2. The dips in pressure and density at ~ 6 kpc are due to the X-ray cavities.

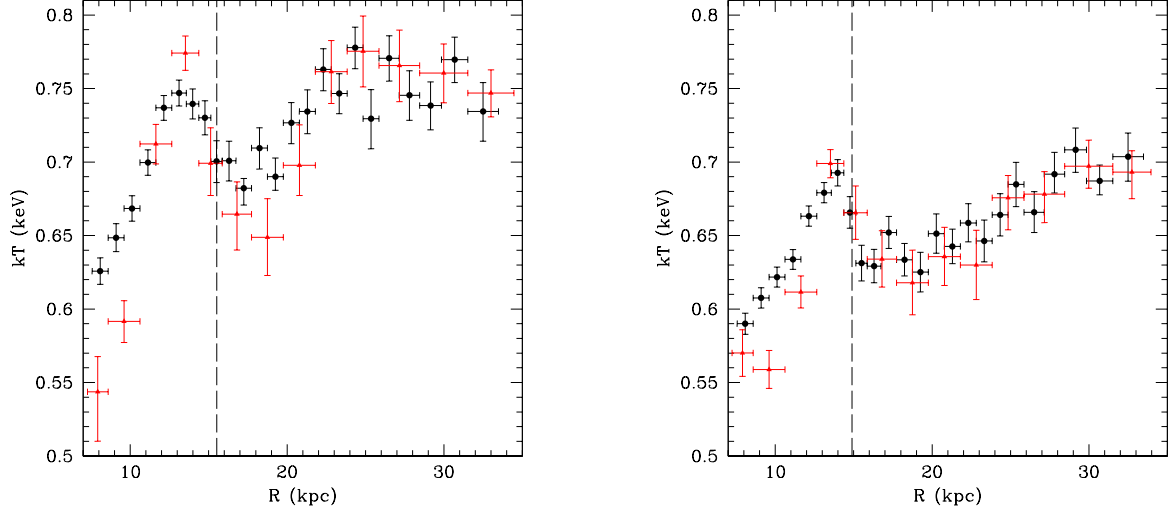


FIG. 11.— Projected (black circles) and deprojected (red triangles) temperature profiles across the northwest (left) and southeastern (right) shocks. Distance is measured from the center of curvature of the corresponding edge and should not be compared with distances in the azimuthally averaged profiles. The dashed lines mark the positions of the density jumps calculated in § 5.1.

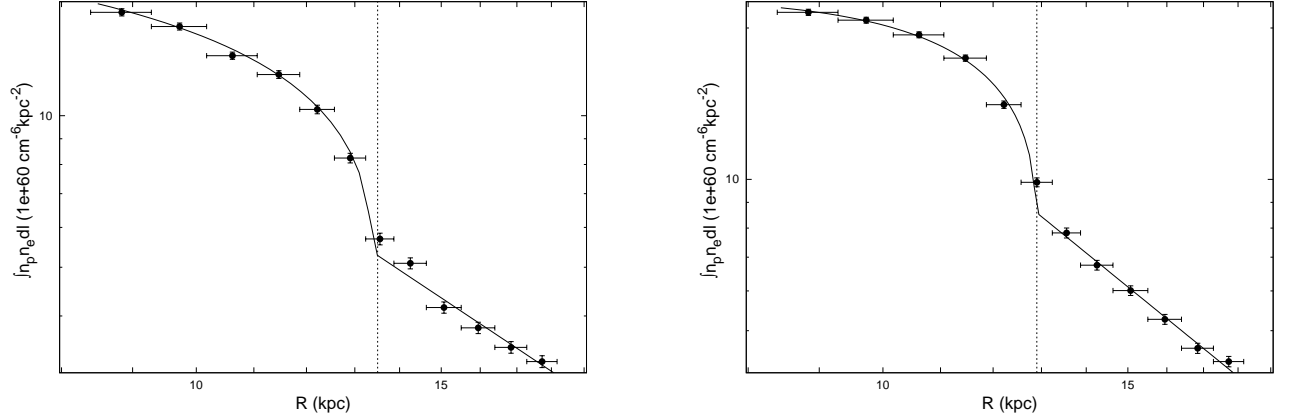


FIG. 12.— Integrated emission measure profiles across the northwest (left) and southeast (right) edges around the middle cavities, indicated in Figure 1. Distances are measured from the center of curvature defined by the shock, not from the central AGN. Each profile shows a sharp edge at ~ 13 kpc. The solid lines show the projected best-fitting discontinuous power-law density models, and the vertical dashed lines mark the best-fitting break radii corresponding to density discontinuities.

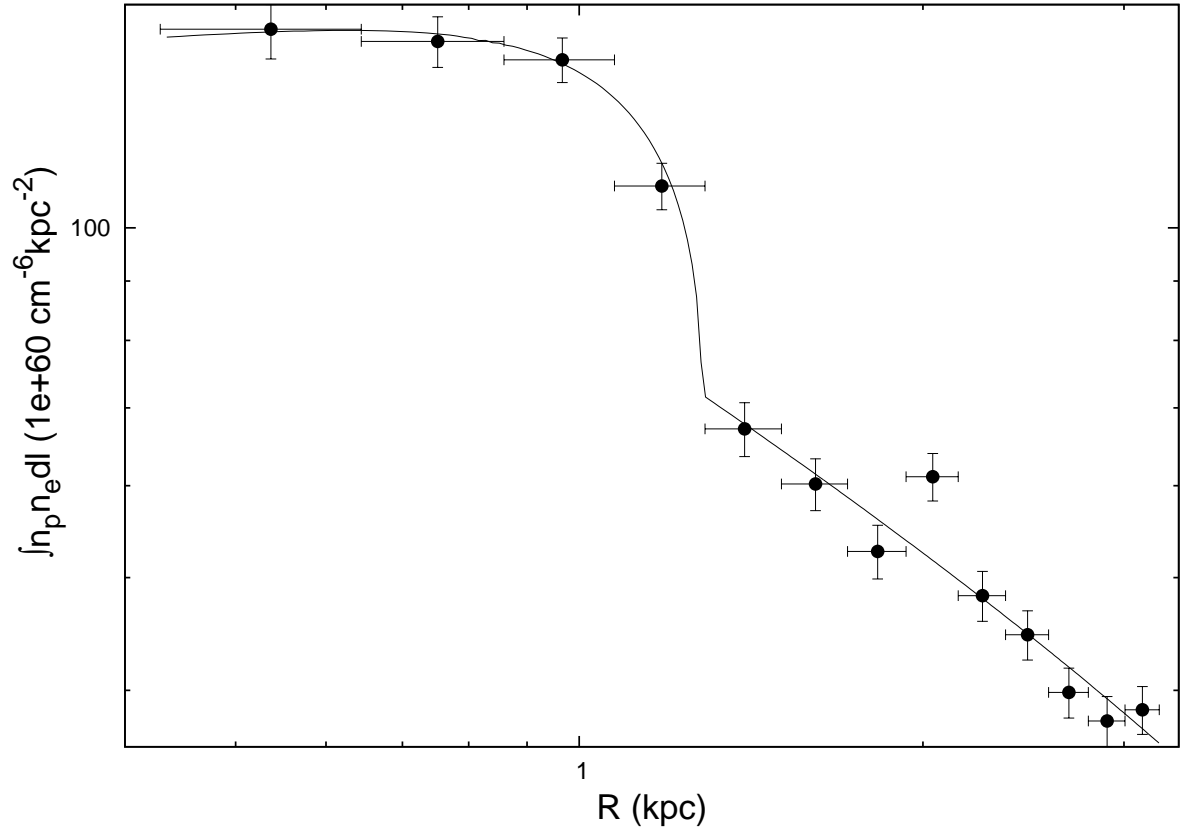


FIG. 13.— Integrated emission measure profile across the 1.5 kpc edge just southeast of the core, most clearly visible in Figure 2, which is coincident with the edge seen in the core temperature map (Figure 8).

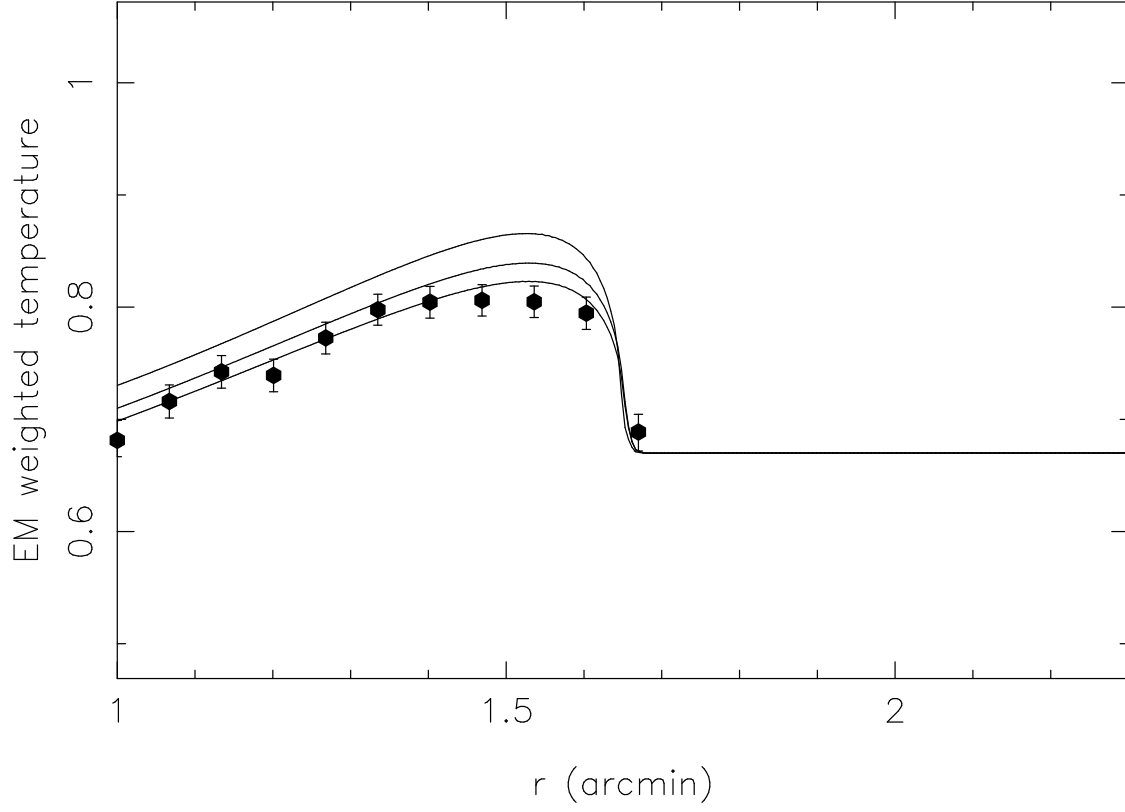


FIG. 14.— Temperature profile from our hydrodynamical simulations of a point explosion in an isothermal sphere, chosen at a time when the corresponding surface brightness profile best matches the observed profile for the northwestern outer shock. The solid lines show the emission-weighted projected temperature profile, with 90% confidence intervals. The points are from results of XSPEC simulations, with the model folded through the *Chandra* response and projected. The predicted projected temperature rise is consistent with what is seen in Figure 11, even though the true temperature rise in the model is larger and consistent with the prediction from 1D shock jumps conditions based on the Mach number.

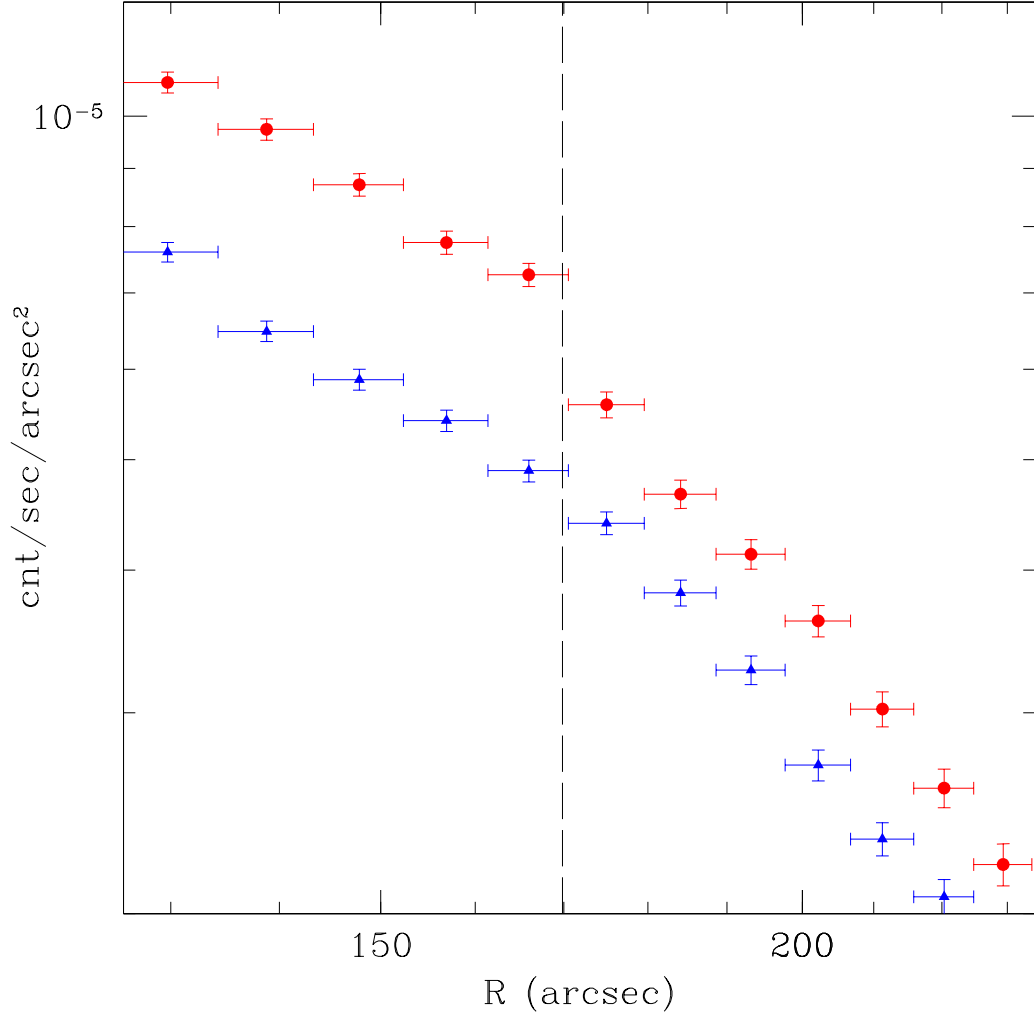


FIG. 15.— 0.3-2.0 keV background-subtracted surface brightness profiles in two wedges across the outer edge indicated in Figure 3 to the northwest (red circles) and south (blue triangles). The northwestern profile was measured between 12° - 79° and the southern profile between 206° - 320° (angles measured from west to north). The northwestern profile shows a jump, followed by a change in slope, at $\sim 170''$ (vertical dashed line), roughly the location of the outer edge. The southern profile also shows a change in slope at $\sim 170''$, though with no associated jump.

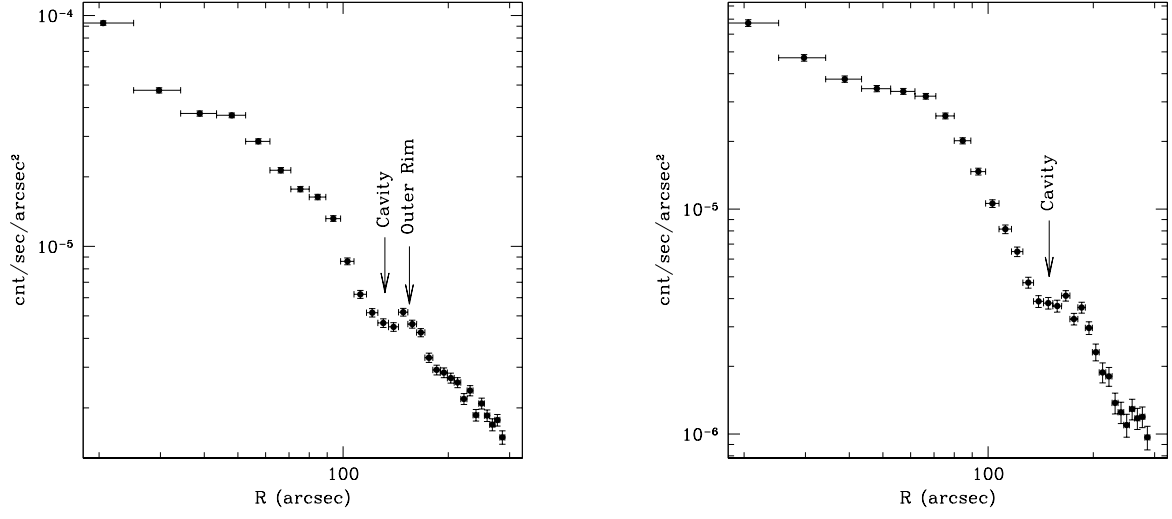


FIG. 16.— 0.3–2.0 keV background subtracted surface brightness profiles across the outer cavities indicated in Figure 3. For the northeastern cavity (left), the profile was extracted between 112° - 153° (measured from west to north), and between 286° - 310° for the southwestern cavity (right). Each profile shows a significant dip at the location of the cavity. For the northeastern cavity, the bright outer rim is also visible.

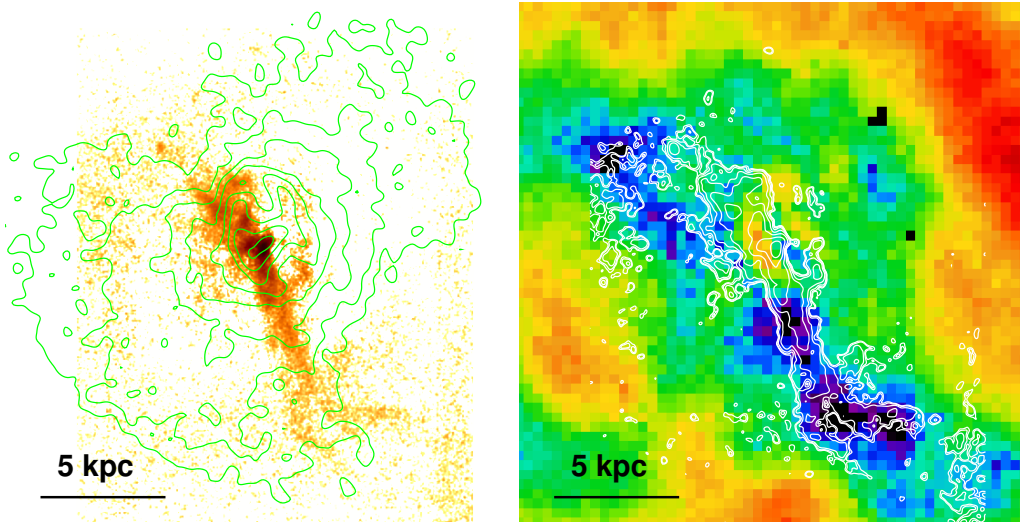


FIG. 17.— *Left:* $H\alpha$ image of the core of NGC 5813 taken with the *SOAR* telescope. The *Chandra* X-ray contours are overlaid in green. The $H\alpha$ filaments extend to the southern edges of the intermediate cavities, and are co-spatial with the trail of cool gas seen in the X-ray temperature map in Figure 6. In the center, the $H\alpha$ emission anti-correlates with the inner X-ray cavities. The image shows the cool $H\alpha$ gas being displaced as the central cavities are inflated, and lifted by the intermediate cavities as they rise buoyantly. *Right:* Close-up of the central part of the temperature map shown in Figure 6, with $H\alpha$ contours overlaid in white. The $H\alpha$ is co-spatial with the cool X-ray filament.